

The primary and secondary instabilities of flow generated by an oscillating circular cylinder

By JOHN R. ELSTON,¹ H. M. BLACKBURN^{1,2}
AND JOHN SHERIDAN¹

¹Department of Mechanical Engineering, PO Box 31, Monash University 3800, Victoria, Australia

²CSIRO Manufacturing and Infrastructure Technology, PO Box 56, Highett 3190, Victoria, Australia

(Received 26 January 2005 and in revised form 7 September 2005)

Two- and three-dimensional instabilities of the two-dimensional symmetric flow generated by a circular cylinder oscillating with simple harmonic motion in quiescent fluid, or, alternatively, by oscillatory flow past a stationary cylinder at low Keulegan–Carpenter and Stokes numbers are investigated via Floquet analysis and direct numerical simulation. Previous experimental visualization has found that the flows produced at low amplitudes and frequencies of motion can be grouped by their visual characteristics into a number of distinct regimes. At low values of Keulegan–Carpenter and Stokes numbers, the flow is two-dimensional and has a reflection symmetry about the axis of oscillation, in addition to a pair of spatio-temporal symmetries. This study isolates and classifies the symmetry-breaking instabilities from these two-dimensional basic states as functions of these control parameters. It is found that while the initial bifurcations produced by increasing the parameters can be to three-dimensional flows, much of the behaviour can be explained in terms of two-dimensional symmetry-breaking instabilities. These have two primary manifestations: at low Stokes numbers, the instability is synchronous with the imposed oscillation, and gives rise to a boomerang-shaped mode, while at higher Stokes numbers, the instability is quasi-periodic, with a well-defined second period, which becomes infinite as Stokes numbers are reduced along the marginal stability boundary, ‘freezing’ the quasi-periodic mode into a synchronous one. These two-dimensional modes are, with further small increase in control parameter, unstable to three-dimensional secondary instabilities, and these are the flows which have been reported in previous experimental studies. In contrast, the mode first reported by Honji (*J. Fluid Mech.* vol. 107, 1981, p. 509), which arises at high Stokes numbers, and lower Keulegan–Carpenter numbers than the two-dimensional quasi-periodic mode, has a three-dimensional primary instability arising directly from the symmetrical two-dimensional basic state.

1. Introduction

An intriguing set of flow structures is generated by a circular cylinder driven in unidirectional simple harmonic motion in quiescent fluid, or equivalently by a cylinder placed in a sinusoidally oscillating flow. These flows are of fundamental interest and the results have potential application to the study of loads on structures immersed in waves or other oscillatory fluid motions. At comparatively low amplitudes and frequencies of motion, the flow is completely symmetrical, synchronous with the imposed motion, and in the long-time average generates secondary steady streaming, as shown e.g. by Tatsuno (1973; see also plate 31 of Van Dyke 1982). This secondary

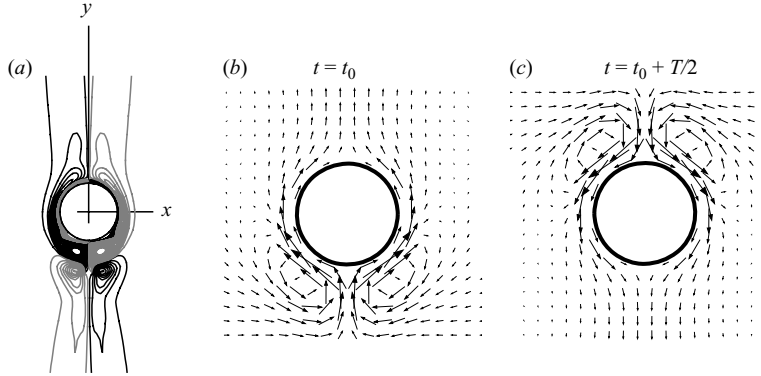


FIGURE 1. Two-dimensional symmetric base flows at low KC and β . (a) The coordinate system (the spanwise, z , coordinate is normal to the (x, y) plane), and contours of positive (black) and negative (grey) vorticity, which have symmetry $(1,6)$. (b, c) The spatial (K_x) and spatio-temporal (H_1, H_2) symmetries of the base flow velocity.

streaming may be qualitatively understood to be driven by time-average low pressures in the high-velocity flows arising near the ‘shoulders’ of the cylinder drawing in fluid from the far field, and which is then driven outwards from the zones of time-average high pressures which arise near the cylinder stagnation points. At higher amplitudes and frequencies, a number of different instabilities arise, producing a variety of flow regimes as demonstrated e.g. in the work of Tatsuno & Bearman (1990). Some of these flows are synchronous with the imposed motion, some have a well-defined second period which is incommensurate with the forcing, so are quasi-periodic, while others exhibit aperiodic switching behaviour in the long term.

In the case of an infinitely long smooth circular cylinder in an infinite extent of fluid, the problem has two dimensionless control parameters. Following convention, we take these to be the Keulegan–Carpenter number

$$KC = 2\pi A/D,$$

and the frequency parameter or Stokes number,

$$\beta = D^2/T\nu,$$

where A is the amplitude of motion, D is the cylinder diameter, T is the period of oscillation and ν is the kinematic viscosity of the fluid. Alternatively one of these groups could be replaced with a Reynolds number; $Re = KC\beta$.

Our purpose in this paper is to analyse the onset of symmetry-breaking instabilities of the time-periodic flows at low-to-moderate values of Keulegan–Carpenter and Stokes numbers, respectively $KC \leq 10$, $\beta \leq 100$.

1.1. Symmetries

We consider bifurcations from T -periodic basic states. At low Keulegan–Carpenter or Stokes numbers, the flow is in its most symmetric state: it has reflection symmetry about the axis of oscillation, translation and reflection invariance in the cylinder axial direction, and in addition has two spatio-temporal symmetries. Fixing the coordinate system to the cylinder axis, as shown in figure 1, we can write the spatial symmetries for the velocity fields of the initial states as

$$x\text{-reflection: } K_x(u, v, w)(x, y, z, t) = (-u, v, w)(-x, y, z, t), \quad (1.1)$$

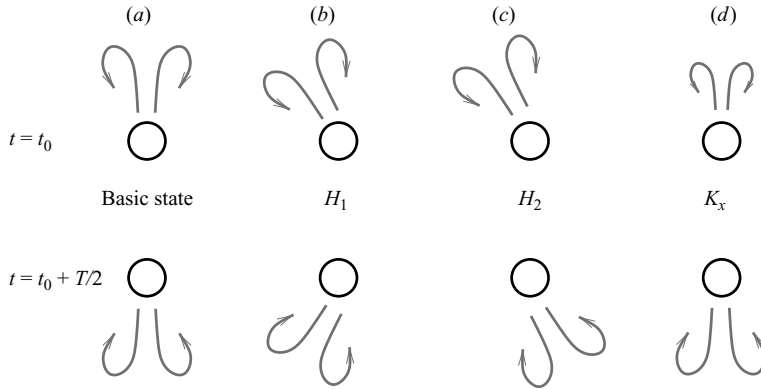


FIGURE 2. Schematics illustrating representative ways in which the two-dimensional symmetries of the basic state can be broken. The basic state, (a), has the three symmetries K_x , H_1 , H_2 , while in (b–d), two out of three break, and the outcomes are labelled with their remaining symmetry.

$$z\text{-translation: } R_\alpha(u, v, w)(x, y, z, t) = (u, v, w)(x, y, z + \alpha, t), \quad (1.2)$$

$$z\text{-reflection: } K_z(u, v, w)(x, y, z, t) = (u, v, -w)(x, y, -z, t), \quad (1.3)$$

a spatio-temporal symmetry:

$$H_1(u, v, w)(x, y, z, t) = (u, -v, w)(x, -y, z, t + T/2), \quad (1.4)$$

and another spatio-temporal symmetry, $K_x H_1 = H_1 K_x$:

$$H_2(u, v, w)(x, y, z, t) = (-u, -v, w)(-x, -y, z, t + T/2). \quad (1.5)$$

The two-dimensional symmetries of the z -vorticity component of the base flow, Ω , corresponding to (1.1), (1.4), (1.5) are

$$\Omega(x, y, z, t) = -\Omega(-x, y, z, t), \quad (1.6)$$

$$\Omega(x, y, z, t) = -\Omega(x, -y, z, t + T/2) \quad (1.7)$$

$$\Omega(x, y, z, t) = \Omega(-x, -y, z, t + T/2). \quad (1.8)$$

Note that although the base flows have only two non-zero velocity components, the symmetries are written with three, as the flow instabilities may be three-dimensional. The reflection invariance about the axis of oscillation (1.1) generates a cyclic group of order two, Z_2 (the same operation, applied twice, is equivalent to the identity). The spatio-temporal symmetries H_1 , H_2 are each isomorphic to Z_2 , and taken together, the three symmetries K_x , H_1 and H_2 generate the group $Z_2 \times Z_2$. Figure 2 illustrates in schematic fashion some possible ways in which the two-dimensional symmetry may break, leaving new two-dimensional flows which have a Z_2 symmetry group. Note that each of the states with broken symmetry represented in the figure is actually one of a pair of alternative states that are related through the broken symmetry.

With the assumption of spanwise periodicity for any three-dimensional behaviour, (1.2) and (1.3) combine to generate a group with $O(2)$ symmetry. The complete symmetry group of the basic state is then $Z_2 \times Z_2 \times O(2)$. In problems with a significant number of symmetries, it is usually the case that successive bifurcations produced by manipulating (typically, increasing) control parameters result in successively more of the symmetries breaking, such that the remaining symmetry group progressively reduces in size (see e.g. Golubitsky, Stewart & Schaeffer 1988).

1.2. Previous investigations

Owing in large part to the practical interest in the forces which are exerted on slender cylindrical structures in oscillatory flows, a number of experimental investigations have previously been undertaken, although in the main these have focused on higher values of Keulegan–Carpenter and Stokes numbers than will be considered here, and often, on flow-induced loads (e.g. Sarpkaya 1986; Obasaju, Bearman & Graham 1988).†

The primary flow visualization studies relevant to instabilities at low KC and β are those of Honji (1981), Williamson (1985) and Tatsuno & Bearman (1990). Analysis related to the Honji instability in the high- β limit was presented by Hall (1984), and this mode has also received renewed experimental attention, again for high Stokes numbers, in the flow visualization work of Sarpkaya (2002).

Honji (1981) demonstrated that for $\beta \in [70, 700]$ and $KC < 2.5$ the flow is subject a three-dimensional instability that breaks the $O(2)$ spanwise symmetry, and which is synchronous with the imposed oscillation. Examination of his visualizations suggests that, while the reflection symmetry K_x is also instantaneously broken at any spanwise plane, the spanwise-averaged patterns preserve it. Flows appear to retain the H_1 symmetry at each spanwise plane. Honji established a (β, KC) -space curve of marginal stability for this three-dimensional mode in the range $\beta \in [70, 700]$, and also a second curve, at higher Keulegan–Carpenter values, at which the mode broke up. At $(\beta = 200, KC = 1/8)$, the spanwise wavelength for his three-dimensional mode was $\lambda = 0.6D$ at onset; in regions of instability this was observed to decrease with increasing β and increase with increasing KC . Honji noted that the instability appeared to be of centrifugal type.

An asymptotic–numerical study of three-dimensional instability of the boundary layer on the oscillating cylinder was performed by Hall (1984), leading to the result

$$KC_c = 5.87 \beta^{-1/4} [1 + 0.21 \beta^{-1/4} + \dots]. \quad (1.9)$$

While his simplified analysis concentrated on high- β regimes, (1.9) provides good estimates for the Keulegan–Carpenter values of the three-dimensional instabilities observed by Honji (1981), down to $\beta \sim 100$. A value for the dimensionless spanwise wavenumber in the high- β limit is supplied, from which the relationship

$$\lambda_c/D = 6.95 \beta^{-1/2} \quad (1.10)$$

may be found; at $\beta = 200$ this also agrees quite well with Honji's measurements. The analysis, and its close correlation with Honji's results, lends strong support to the idea that the three-dimensional instabilities observed by Honji are produced by centrifugal instability in the boundary layer flow past the oscillating cylinder.

Williamson (1985) concentrated on two-dimensional features of flow instabilities via free-surface flow visualization and force measurements, primarily for $KC \leq 35$ and $\beta = 255$ (we note that at $\beta = 255$, (1.9) predicts the onset of three-dimensional instability at $KC = 1.546$, so the flows studied by Williamson would have had significant three-dimensionality). An interesting feature of that work was the generation of more pairs of shed vortices per motion cycle as KC was increased, up to four pairs per cycle at $KC \sim 35$. The pairing of vortices produced during a half-cycle to those generated in the following half-cycle resulted in a number of distinct

† For work relating to flows around and loadings on surface-piercing cylinders in wave (as opposed to unidirectional oscillatory) flows, see Yang & Rockwell (2002, 2004).

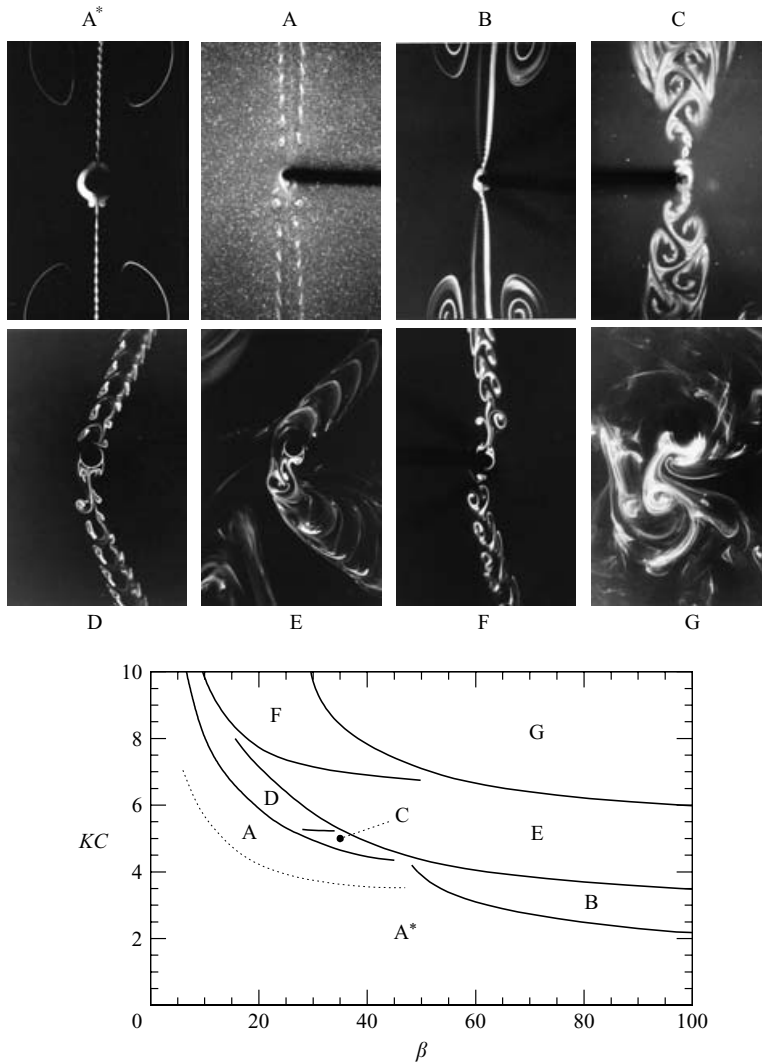


FIGURE 3. Classification of symmetry-breaking flows in the $\beta \in [0, 100] \times KC \in [0, 10]$ subset of control space according to Tatsuno & Bearman (1990). The image for regime F appeared in Tatsuno & Bearman (1988), while the others are from Tatsuno & Bearman (1990); all are reproduced with the permission of the authors.

surface flow patterns. Williamson identified the following vortex shedding regimes: pairing of attached vortices ($KC < 7$); transverse vortex street ($KC \in [7, 13]$); single pairs of vortices ($KC \in [13, 15]$); two pairs ($KC \in [15, 24]$); three pairs ($KC \in [24, 32]$) and four pairs ($KC > 32$) per motion cycle.

The most comprehensive visualization study of symmetry-breaking instabilities thus far presented for this flow is that of Tatsuno & Bearman (1990). Their work used vertical circular cylinders that pierced the free surface of water in test tanks and which were driven horizontally in simple harmonic motion. Based on dye-release and free-surface streakline visualization, they produced a (β, KC) -space map of eight different regimes found for $\beta \in [5, 150]$, $KC \in [1.6, 15]$, the main portion of which is reproduced here, together with sample flow visualizations, in figure 3. We will use

their nomenclature in much of the following. Flows of regimes A and A* preserve full symmetry. The distinction between regimes A and A* was described by Tatsuno & Bearman as being that flows of regime A* did not apparently produce vortex shedding, although dye could still be transported away from the cylinder along the axis of motion for regime A*. On the other hand, Tatsuno & Bearman noted that even for regime A, the far-field concentrations of dye do not represent vortices, but instead mark periodic mass convection from the surface of the cylinder; shed vortices are confined to a region near the surface of the cylinder.

A key observation is that the flows in all the symmetry-breaking regimes (B–G) were apparently three-dimensional, as well as breaking two-dimensional symmetry. Flows in regime B correspond to those found by Honji (1981). The indication of reflection symmetry about the y -axis for the dye visualization seen in figure 3 in fact derives from three-dimensional structure in the page-normal direction. Flows in regimes C–G are distinguished from those of regime B by fundamentally two-dimensional symmetry breaking, in addition to being three-dimensional: the spanwise average of the flows cannot be considered to preserve K_x , while this is the case for regime B.

Flows in regimes D and F were apparently synchronous with the motion of the cylinder, although detailed examination of the relevant images in figure 3 suggests that in fact regime F is not completely synchronous. Considering just the two-dimensional symmetries K_x , H_1 and H_2 , flows of regime D break K_x and H_2 but preserve H_1 , while those of F break K_x and H_1 but preserve H_2 . Flows of regime D produce two obliquely arranged vortex streets, each disposed either on the positive- or negative- x side of the cylinder, while F has the same symmetries as Williamson's two-pairs mode, and produces a diagonally opposed pair of vortex streets.

Flows in regime C lose synchronicity with the motion of the cylinder, but evidently gain a new secondary period associated with the production of large vortices arranged in opposed Kármán-jet-type arrays, one emanating in the $+y$ -direction, the other in $-y$. The flows of regime C are thus quasi-periodic. When viewed normal to the plane of cylinder oscillation, the shedding appears to be slantwise (see the chevron-type patterns in figure 15, Tatsuno & Bearman 1990), although, as for the low-Reynolds-number wake of the cylinder in cross-flow, leaving open the possibility that this behaviour could be related to end effects.

Flows in regime E appear to have some similarity with those of regime D, except that the oblique directions in which the flow convects away from the cylinder switch intermittently from $+x$ to $-x$ sides of the cylinder. Flows of regime G are distinctly chaotic, and generate large-scale circulatory flow around the cylinder, which intermittently reverses direction.

More recently, Sarpkaya (2002) extended the work of Honji (1981) to much higher Stokes numbers ($\beta_{\max} = 1.4 \times 10^6$), and supplied new correlations for the Stokes-number dependence of Keulegan–Carpenter number and spanwise wavelength at the onset of low- KC three-dimensional instabilities, specifically

$$KC_c = 12.5 \beta^{-2/5}, \quad \lambda_c/D = 22 \beta^{-3/5}, \quad (1.11)$$

where the value for KC_c agrees with (1.9) at $\beta \approx 100$, then gives lower values at greater Stokes numbers, while the correlation for λ_c agrees with (1.10) for $\beta \approx 1 \times 10^5$, and gives higher values at lower KC . Further comparisons of the various experimental and analytical results for the Honji instability mode will be presented in §5.

Previous numerical investigations have largely been confined to examination of two-dimensional flows. In regard to the onset of two-dimensional symmetry breaking,

Justesen (1991) noted that at high Stokes numbers, two-dimensional flows were unstable to asymmetric perturbations above a boundary that coincided with $KC \approx \pi$ at $\beta \approx 200$, falling as Stokes numbers increased. Iliadis & Anagnostopoulos (1998) located a boundary in (β, KC) -space between two-dimensional flows which preserve and break the K_x symmetry. At Stokes numbers above approximately 40, this conformed reasonably well with the B–E boundary found by Tatsuno & Bearman (1990) (which marks a fundamentally two-dimensional transition), but at lower Stokes numbers it departed increasingly from the A–D boundary. At low Stokes numbers, flows which obviously correspond to the two-dimensional equivalents of regimes D (here at $KC = 2\pi$, $\beta = 22.1$ and 25.6 , although the latter, according to Tatsuno & Bearman's regime boundaries, would have been just inside regime E) and F ($KC = 10$, $\beta = 20$) were identified. In both cases the flow was stated to be completely periodic and synchronous with the cylinder oscillation, although detailed examination of force time series presented in their figure 20 suggests this was not strictly true of the regime F flow. Also in 1998, Dütsch *et al.* presented further two-dimensional computations and also Laser-Doppler anemometry data for regimes A, E and F, where, in part, it was established that regime F is asynchronous for both (three-dimensional) experiment and two-dimensional computations. In none of the above studies was the precise nature (e.g. temporal characteristics) of the primary two-dimensional symmetry breaking that occurs at high Stokes numbers established.

Recently, three-dimensional direct numerical simulation (DNS) studies have begun to appear, for example that of Nehari, Armenio & Ballo (2004). That work examines two three-dimensional states, both at $\beta = 20$, one at $KC = 6.5$ (regime D) and the other at $KC = 8.5$ (regime F). The simulation domain size ($\Delta x = 14D$, $\Delta y = 26D$, $\Delta z = 12D$) was comparatively small in $(x-y)$ extent, although large enough to contain a small number of spanwise wavelengths of regime D ($\lambda/D \sim 4$ in figure 22, Tatsuno & Bearman 1990) or regime F ($\lambda/D \sim 5$, figure 30). One fundamental feature of both sets of simulations was that the underlying broken two-dimensional symmetry of the three-dimensional states was observed to change signs (apparently irregularly) over the course of the simulation. Particularly for the flow of regime D, this switching was found to profoundly affect the spanwise wavenumber distribution of energy over time, disrupting the initially good spanwise organization at the expected wavelength. This switching had not previously been reported for either of regimes D or F, although it was certainly a defining characteristic of regime E – and also, as will be seen later, of regime C, although in this case the oscillation has a well-defined periodicity. The switching was reproduced by two-dimensional simulations, also with another two-dimensional simulation code and at higher resolutions. The spanwise modulation of the three-dimensional wavelengths resulting from two-dimensional switching appears to be related to the long-wavelength sinusoid noted by Yang & Rockwell (2002) in wave (orbital) flows.

In this problem, with a pair of control parameters and a number of distinct flow regimes, it becomes computationally expensive to map out regime/stability boundaries, or, particularly for three-dimensional simulations, to examine more than a few points in control space. In addition, appropriate spanwise domain extents may be difficult to set in the absence of guiding experimental data. Naturally, experimental investigations of the type mounted by Tatsuno & Bearman afford the most rapid way of differentiating flow regimes, but when a number of competing modes may exist in a small region of control space (e.g. in the present problem, near $KC = 4.5$, $\beta = 45$) and particularly when one wishes to isolate the impact of two-dimensional, as opposed to three-dimensional, instabilities, computational approaches are very useful.

Stability analysis is an appropriate investigative tool here, at least when attempting to establish the nature of instabilities of steady or periodic basic states.

In Elston, Sheridan & Blackburn (2004), the present authors demonstrated that Floquet analysis could be used to study symmetry breaking in this problem for flows restricted to a two-dimensional subspace. It was shown that there is a single curve of marginal stability in (β, KC) -space that accounts for the A–D and A–C transitions (actually, their two-dimensional counterparts), the distinction being based on the type of bifurcation that arises. Floquet multipliers for the A–D transition are real ($\mu = +1$ at criticality), leading to new flows synchronous with the cylinder oscillation, while those for the A–C transition occur in complex-conjugate pairs ($\mu = \exp \pm i\theta$). The A–C transition occurs through a Neimark–Sacker bifurcation, with the imaginary part of the multipliers related to a new secondary period, T_s , leading to states which are quasi-periodic. These findings will be revisited in greater depth here in §3.

Finally we should point out that when the spatio-temporal symmetry of the forcing is broken, this feature may carry over to the base flows as well. This result was established by Tatsuno (1981), who considered the steady streaming at low (β, KC) values, but with time-asymmetrical sawtooth forcing.

1.3. Objectives and approach

The present work expands on our earlier two-dimensional study, by giving greater depth and detail – for example, information quantifying the influence of β on secondary periods for bifurcations to regime C – and also considers three-dimensional instabilities. Since there is a number of transitions between regimes to be dealt with, we have, in the main, restricted attention to parameter values close to the primary symmetry breakings, i.e. A–D, A–C, A*–B, in the ranges $\beta \in [0, 100]$ and $KC \in [0, 10]$.

This is a numerical study, employing both Floquet analysis and DNS. In §2 we describe the numerical methods employed, and give details of convergence testing. Then in §3 we examine two-dimensional instabilities of the basic states, followed by §4 where three-dimensional instabilities of both two-dimensional flows with enforced symmetry and of states such as C and D that have broken two-dimensional symmetry are dealt with. When dealing with three-dimensional flows of regime C, where the two-dimensional basic state is quasi-periodic (at present precluding the use of Floquet analysis), we have resorted directly to DNS, and necessarily limited the range of parameters investigated. In §§5 and 6 we discuss and summarize our findings.

2. Computational methods

2.1. Floquet analysis

Temporal Floquet stability analysis examines the behaviour of a perturbation, \mathbf{u}' , to a T -periodic (limit cycle) base flow, \mathbf{U} , to determine whether the perturbation grows or decays from cycle to cycle. In a linear analysis, the evolution equations for the perturbation flow are the Navier–Stokes equations linearized about the base flow. Perturbation solutions can be written as a sum of components $\tilde{\mathbf{u}}(t_0) \exp \sigma(t - t_0)$ where $\tilde{\mathbf{u}}(t_0)$ is a T -periodic Floquet eigenfunction, evaluated at arbitrary phase t_0 , and σ is a Floquet exponent. The Floquet multipliers μ are related to the Floquet exponents σ by $\mu = \exp \sigma T$. In general, the exponents, the multipliers, and the eigenfunctions can either be real, or occur in complex-conjugate pairs. Instability occurs when a multiplier leaves the unit circle, $|\mu| > 1$, or equivalently when the real part of a Floquet exponent becomes positive.

The numerical method used here closely follows that described by Barkley & Henderson (1996) and Tuckerman & Barkley (2000). Its adaptation and application to the two-dimensional subspace of this flow was detailed in Elston *et al.* (2004). If required, the reflection symmetry (1.1) of the base flow is enforced by solving in a half-domain, $x \geq 0$, with symmetry conditions along the $x=0$ boundary. As noted by Elston *et al.*, for two-dimensional Floquet analysis in the current problem there is difficulty resolving stable modes, $|\mu| < 1$. This arises because, while the base flow is driven, not autonomous, it is quite close to being in simple harmonic motion over much of the analysis domain. A simple harmonic motion can arise as the solution of a set of autonomous ODEs, and hence, following the arguments in Iooss & Joseph (1990, §VII.6.2), it has a neutrally stable multiplier, $\mu = +1$. In regions of control space where stable Floquet modes would exist, a spurious multiplier, magnitude just less than unity, always arises in our two-dimensional analyses as a consequence. However, unstable modes are resolved without difficulty, and the location of marginal stability can be estimated by extrapolation to $|\mu|=1$. Examples of this procedure are shown in Elston *et al.* (2004). The difficulty does not arise for three-dimensional modes relatively remote from the two-dimensional subspace.

2.2. Temporal and spatial discretization

Spatial discretization was carried out with two-dimensional quadrilateral spectral elements employing tensor-product Lagrange interpolant shape functions based on Gauss–Lobatto–Legendre quadrature points (the ‘nodal’ basis functions). Time-integration for both the linearized and full Navier–Stokes equations is carried out in primitive variables, with equal-order interpolants for the velocity and pressure, using a velocity-correction scheme (Karniadakis, Israeli & Orszag 1991). In all the analysis and simulation described here, second-order-time integration was employed, and at the time-step sizes required to meet the CFL stability criterion, spatial convergence is the dominant consideration. On all domain boundaries we used, for DNS, a combination of Dirichlet velocity boundary conditions and high-order Neumann pressure boundary conditions adapted for domain motion, as described by Blackburn & Henderson (1999), while for Floquet analysis we combined zero-Dirichlet velocity boundary conditions with high-order pressure boundary conditions.

For three-dimensional direct numerical simulation, the planar discretization into spectral elements is coupled with Fourier expansions in the out-of-plane direction (Karniadakis 1990).

Figure 4 shows example domains and spectral element meshes used for checking the effects of domain size, number of elements (N_{el}), and one-dimensional Lagrange interpolant order (N_p) on both base flows and Floquet analysis results. For each mesh, the radial thickness of the inner layer of elements was $0.1 D$, with 16 elements around the circumference of the cylinder; with $N_p = 8$ this gives 128 independent mesh points on an azimuthal traverse.

2.3. Convergence and domain-size sensitivity checks

2.3.1. Base flows

The diagnostic used to assess base flows was the peak coefficient of force exerted on the cylinder, $\widehat{C}_{fy} = 2\widehat{f}_y/\rho U_{ms} D$, where \widehat{f}_y is the peak total (pressure + viscous) y -component force per unit length, U_{ms} is the mean-square cylinder velocity, and ρ is the density of the fluid. For all tests, the base flows had K_x -symmetry, which was enforced if required by computing on a half-domain.

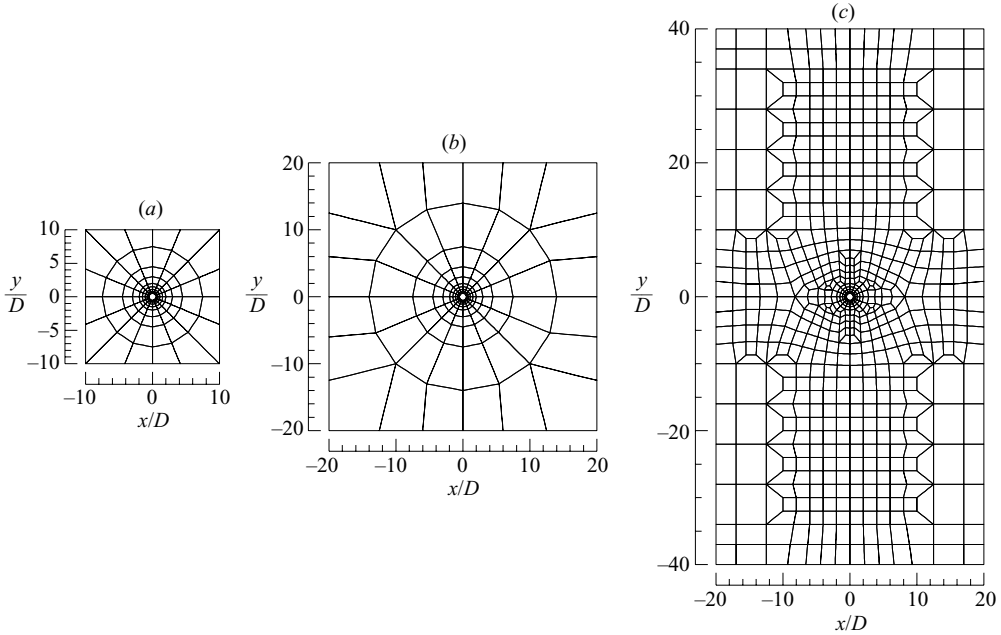


FIGURE 4. Outlines of (a) 144-element $20D \times 20D$ domain; (b) 164-element $40D \times 40D$ domain used to compute the majority of the results reported here; (c) 700-element $40D \times 80D$ domain. At interpolant order $N_p = 8$, these meshes have respectively 9344, 10 656 and 45 136 grid points.

Domain size, N_{el}	$20D \times 20D$, 144	$40D \times 40D$, 164	$60D \times 60D$, 192	$80D \times 80D$, 192
\widehat{C}_{fy}	9.717	9.687	9.682	9.678

TABLE 1. Peak coefficients of y -component force per unit length for different domain sizes and number of elements, with the order of the tensor-product interpolant function employed within each element held constant at $N_p = 8$. Simulations performed at $(\beta = 100, KC = 2.5)$. Figure 4(a, b) illustrates two meshes in the family employed for these tests.

	$(\beta, KC) \setminus N_p$	6	8	10	12
(a)	(12.5, 8)	5.433	5.434	5.434	5.434
	(40, 4.5)	6.080	6.080	6.080	6.080
	(100, 2.5)	9.687	9.687	9.687	9.686
(b)	(12.5, 8)	5.420	5.420	5.420	5.420
	(100, 2.5)	9.682	9.682	9.681	9.681

TABLE 2. N_p -convergence results for peak coefficients of y -component force per unit length, \widehat{C}_{fy} , obtained using (a) the 164-element, $40D \times 40D$ mesh (figure 4b), and (b) the 700-element, $40D \times 80D$ mesh (figure 4c). Simulations at $(\beta = 12.5, KC = 8)$ conducted with enforced K_x symmetry.

An investigation of domain size effects on \widehat{C}_f at one point in (β, KC) -control space for a family of meshes like those of figure 4(a, b), and at a fixed interpolant order, $N_p = 8$, is shown in table 1. The results of table 2 demonstrate N_p convergence on meshes figure 4(b, c) for various locations in (β, KC) . These results suggest that

(a)	$(\beta, KC) \setminus N_p$	6	8	10	12
	(40, 4.75)	1.1088	1.1064	1.1064	1.1057
	(100, 3.65)	1.1472	1.1473	1.1471	1.1468
(b)	$(\beta, KC) \setminus$ Domain size	$20D \times 20D$	$40D \times 40D$	$60D \times 60D$	$80D \times 80D$
	(40, 4.75)	1.1035	1.1064	1.1239	1.1282
	(100, 3.65)	1.1102	1.1473	1.1448	1.1429

TABLE 3. Floquet analysis results for two-dimensional symmetry breaking. (a) N_p -convergence of $|\mu|$ on the $40D \times 40D$ domain (figure 4b) at two locations in control space; (b) domain-size sensitivity of $|\mu|$ at $N_p = 8$.

domain size effects are not significant for domains of size $40D \times 40D$ and above, and also that $N_p = 8$ is sufficient to produce results that are converged to four-figure accuracy.

2.3.2. Floquet analysis

Effects of interpolant order and domain size on Floquet multiplier magnitude for a two-dimensional symmetry-breaking flow at $(\beta = 40, KC = 4.75)$ and $(100, 3.65)$ are shown in table 3. By comparison to tables 1 and 2 it will be seen that the convergence properties of Floquet multipliers are quite similar to those for the force coefficient. The convergence properties for three-dimensional and two-dimensional Floquet analyses are effectively the same.

In the present work, typically 64 time slices of the base-flow limit cycle, equi-spaced in time over period T , were supplied to the Floquet solver for reconstruction of the base flow. Testing at selected (β, KC) showed that the computed multipliers were typically the same to four significant figures at half this number of slices.

2.3.3. Outcome

On the basis of the testing outlined above, a domain extent of $40D \times 40D$ and interpolant order $N_p = 8$ were selected to compute most of the results reported here. Many results have been cross-checked on the $40D \times 80D$, 700-element mesh of figure 4(c), also at $N_p = 8$. In all Floquet analysis, 64 time slices have been employed for Fourier reconstruction of the base flows.

3. Two-dimensional symmetry breaking

With a restriction to a two-dimensional subspace, Floquet modes will break two of the three symmetries (1.1), (1.4), (1.5). Within the range of control-space parameters investigated here ($\beta \leq 100, KC \leq 10$), a single curve of marginal stability has been identified, but there are two distinct types of behaviour, depending on whether the critical Floquet multipliers are real and positive, or occur in complex-conjugate pairs (Elston *et al.* 2004). The curve of marginal stability is shown in figure 5(a). At low Stokes numbers, $\mu_c = +1$, leading to two-dimensional instabilities that are synchronous with the base flow; these are labelled ‘S’. At higher Stokes numbers, $\mu_c = \exp \pm i\theta$, leading to quasi-periodic instabilities, labelled ‘QP’. It can also be seen that there is a very close correspondence between the curve of marginal stability and an amalgam of some of the regime boundaries observed by Tatsuno & Bearman (1990). (However, we maintain a separate nomenclature S/QP in order to distinguish between the two-dimensional-subspace modes and the three-dimensional regimes identified by

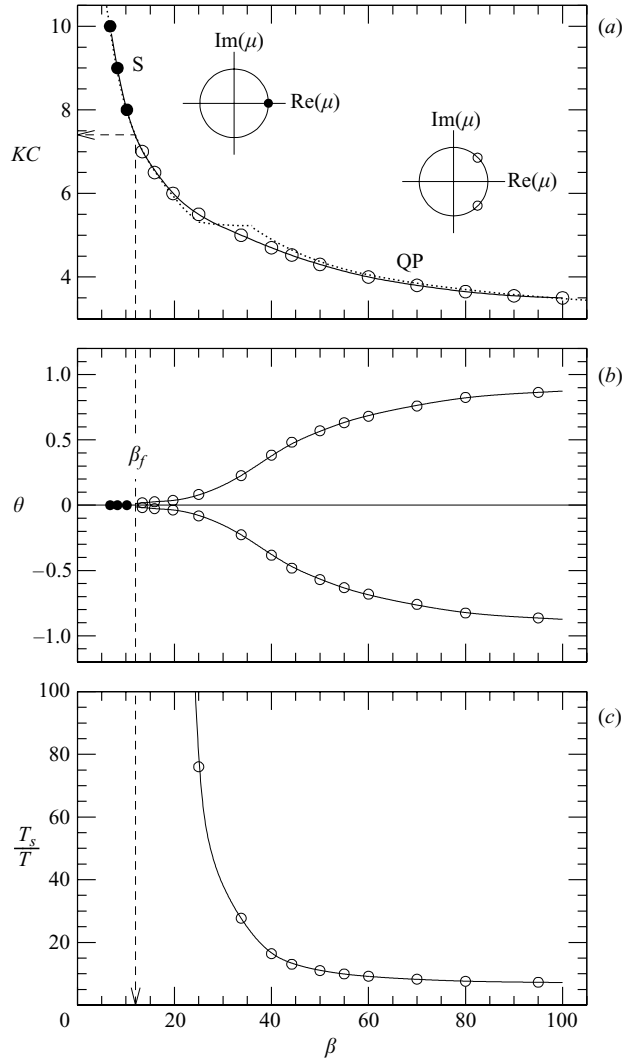


FIGURE 5. Outcomes of Floquet analysis for two-dimensional flows. (a) The curve of marginal stability in (β, KC) control space, with insets illustrating the placement of critical multipliers on the unit circle in the complex domain. In regime S (●), real multipliers cross the unit circle at $\mu = +1$, while in regime QP (○), critical multipliers occur in complex-conjugate pairs (again with $|\mu| = 1$). Boundaries for the transitions A–D, C–D and B–E from Tatsuno & Bearman (1990) are indicated by the dotted line. (b) The phase angles of the multipliers, and (c) the ratios of the corresponding secondary periods T_s to those of the base flows, T , both as functions of β . Dashed lines indicate approximate values of β_f and KC_f for the change from real to complex-conjugate pair multipliers.

Tatsuno & Bearman.) At low Stokes numbers, the two-dimensional curve agrees with the three-dimensional A–D boundary; at high Stokes numbers it agrees with the B–E boundary, where we note that for the experiments, the corresponding base state is already three-dimensional, while at $\beta \sim 30$ where agreement with the other boundaries weakens, the C–D boundary crosses our curve.

The phase angles θ of the critical multipliers $\mu = \exp \pm i\theta$ are plotted as a function of β in figure 5(b), where it can be seen that the transition from complex-conjugate pair

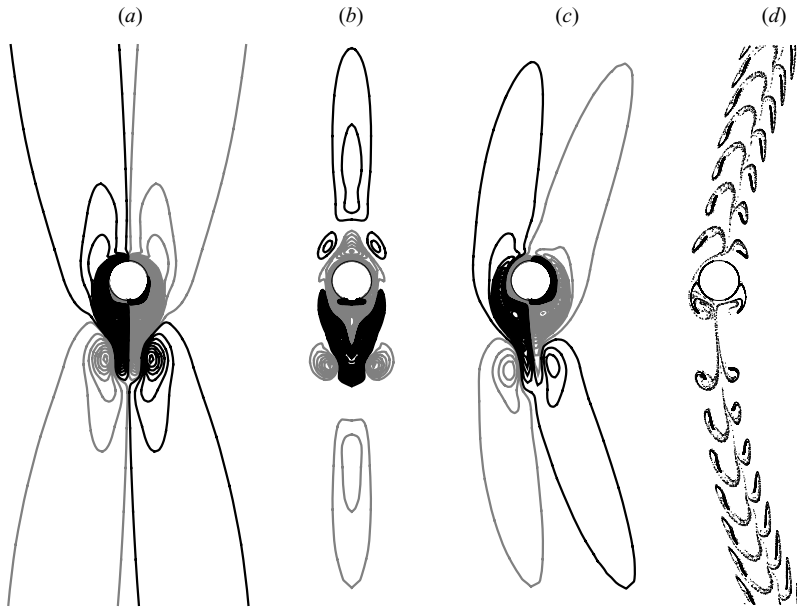


FIGURE 6. Flows of two-dimensional synchronous regime S, computed at ($\beta = 13.75$, $KC = 7$): (a) instantaneous vorticity contours for the basic state, with the cylinder at $y = y_{\max}$; (b) vorticity contours of the Floquet eigenfunction at the same phase of the motion cycle; (c) instantaneous vorticity contours obtained from two-dimensional DNS, again at $y = y_{\max}$; (d) computed positions of massless particles advected from close to the cylinder.

to real multipliers (regime QP to regime S) occurs as the angles asymptote to zero. At this location, the quasi-periodic mode ‘freezes’ into a synchronous one. Consequently, it is difficult to specify the exact location of transition, but a convenient value is $\beta_f \approx 12$. By extrapolation onto figure 5(a), we find the corresponding $KC_f \approx 7.4$ (oscillation amplitude $1.18D$).

For the quasi-periodic modes, a new secondary period T_s arises, associated with the phase angle θ of the multipliers. The relationship between θ and T_s is not necessarily direct, since the phase angles are not necessarily the winding numbers corresponding to the secondary periods; they are winding numbers modulo 2π . However, in Elston *et al.* (2004) we showed by comparison to two-dimensional DNS results that for the present case, the simple relationship $T_s/T = 2\pi/\theta$ holds. Figure 5(c) shows the ratios T_s/T derived from the critical Floquet multipliers. As $\beta \rightarrow \beta_c^+$, $T_s/T \rightarrow \infty$, while for $\beta \rightarrow 100$, $T_s/T \rightarrow 7$ approximately.

We emphasize that figure 5 is not a bifurcation diagram in the conventional sense, but shows instead the behaviour of critical Floquet multipliers along a traverse of the marginal stability curve in the two-dimensional (β , KC) control space. Further, it supplies no information on the two-dimensional extents of the S and QP regimes.

3.1. Two-dimensional synchronous regime S

Figure 6 illustrates the nature of the synchronous modes. In figure 6(a) we see instantaneous vorticity contours for the base flow at ($\beta = 13.75$, $KC = 7$), for the time at which the cylinder is at its maximum displacement in the y -direction. Figure 6(b) shows the vorticity contours of a Floquet eigenfunction at the same phase in the motion cycle. The eigenfunction vorticity replaces the odd x -symmetry of the base-flow vorticity (1.6) with an even symmetry, and consequently the flow that results from

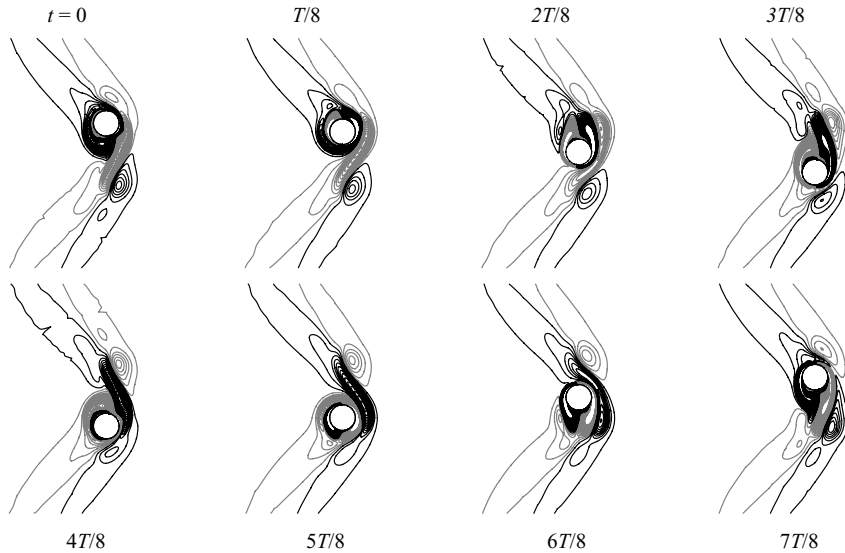


FIGURE 7. A sequence of instantaneous vorticity contours for the synchronous two-dimensional flow of regime S, computed at ($\beta = 15$, $KC = 7$), at eight phases of the motion period T . At $t = 0$, the cylinder is at y_{\max} .

the interaction (figure 6c) breaks (1.6), or, in velocity variables, (1.1). The reflection symmetry can break in two ways, corresponding to changing the sign of the vorticity eigenfunction in figure 6(b), but the centre manifold is one-dimensional, with a single real Floquet multiplier. In figure 6(c) vorticity contours for the saturated (self-limiting, asymptotic) flow obtained at the same point in control space are shown, computed using two-dimensional DNS initiated with the base flow perturbed by the leading Floquet eigenfunction. The vorticity contours have a characteristic ‘boomerang’ or V shape.

The particle-track plot of figure 6(d) bears a great deal of similarity to Tatsuno & Bearman’s flow visualization for regime D, see figure 3. A point of interest here is that while the particle-track plot suggests vortex shedding, with associated far-field concentrations of vorticity, in fact the far-field vorticity distribution is very smooth; only quite close to the cylinder is there any sensible indication of vortex shedding. Similar observations were made by Tatsuno & Bearman in relation to flows of regime A.

A sequence of instantaneous vorticity contours extracted over one motion cycle from saturated DNS at ($\beta = 15$, $KC = 7$), still in regime S (figure 7), shows that while the reflection symmetry is broken, the flow retains the spatio-temporal symmetry (1.7), or equivalently, $H_1 -$ and the flow resembles the schematic figure 2(b). Compared to the flow shown in figure 6(c), the flow here breaks symmetry in the opposite sense, being arbitrarily dependent on initial conditions. Also, at the slightly higher value of $\beta = 15$, cf. $\beta = 13.75$ in figure 6, the angle of deviation of the flow from the y -axis has increased.

A point of interest is that for the analysis and flows illustrated both in figure 6 where ($\beta = 13.75$, $KC = 7$) and figure 7 where ($\beta = 15$, $KC = 7$), we have control-space coordinates with Stokes numbers higher than, and Keulegan–Carpenter numbers lower than, the location of the ‘freezing point’ on the marginal stability curve (see

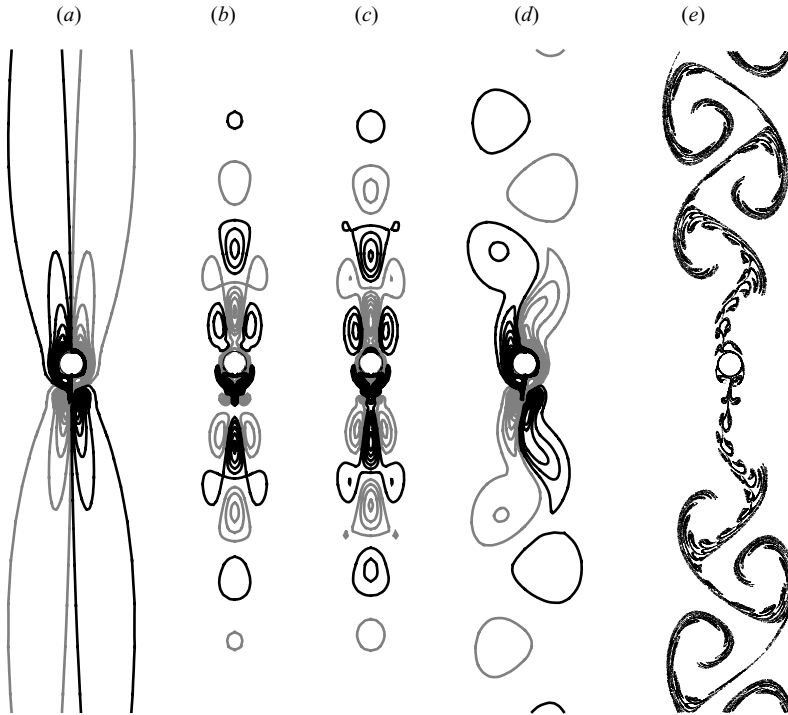


FIGURE 8. Flows of two-dimensional quasi-periodic regime QP, computed at ($\beta=40$, $KC=4.7$): (a) instantaneous vorticity contours for the basic state, with the cylinder at $y=y_{\max}$; (b, c) vorticity contours of the real and imaginary parts of the Floquet eigenfunction at the same phase of the motion cycle; (d) instantaneous vorticity contours obtained from two-dimensional DNS, again at $y=y_{\max}$; (e) computed positions of massless particles advected from close to the cylinder.

figure 5: $\beta_f \approx 12$, $KC_f \approx 7.4$). Finally, we note that our two-dimensional saturated states of regime S are completely periodic, over many oscillation cycles.

3.2. Two-dimensional quasi-periodic regime QP

Figure 8(a) illustrates the base flow for ($\beta=40$, $KC=4.7$) at the instant when the cylinder is at its maximum y displacement, while figures 8(b) and 8(c) respectively show the real and imaginary parts of the critical Floquet eigenfunction at the same phase point. The base flows and the eigenfunctions have the same symmetries as for the cases with real multipliers – again, the eigenfunctions break the reflection symmetry (1.1), (1.6). In figure 8(d) we see instantaneous vorticity contours extracted from saturated DNS, which shows the vortex shedding that occurs at the secondary period T_s . In contrast with a conventional planar Kármán wake, the signs of rotation associated with concentrations of vorticity are reversed: we have a pair of phase-locked Kármán-street planar jets. An image of structures formed by particle tracking is shown in figure 8(e). Note the immediate similarity with Tatsuno & Bearman's flow visualization for regime C (see figure 3), and also, by comparison with figure 8(d), the relationship between far-field concentrations of vorticity and advected particle locations.

Both Floquet multipliers and eigenfunctions occur in complex-conjugate pairs for quasi-periodic modes; figure 8(b, c) shows the real and imaginary parts of the eigenfunction, normalized to the same energy level. The information contained in

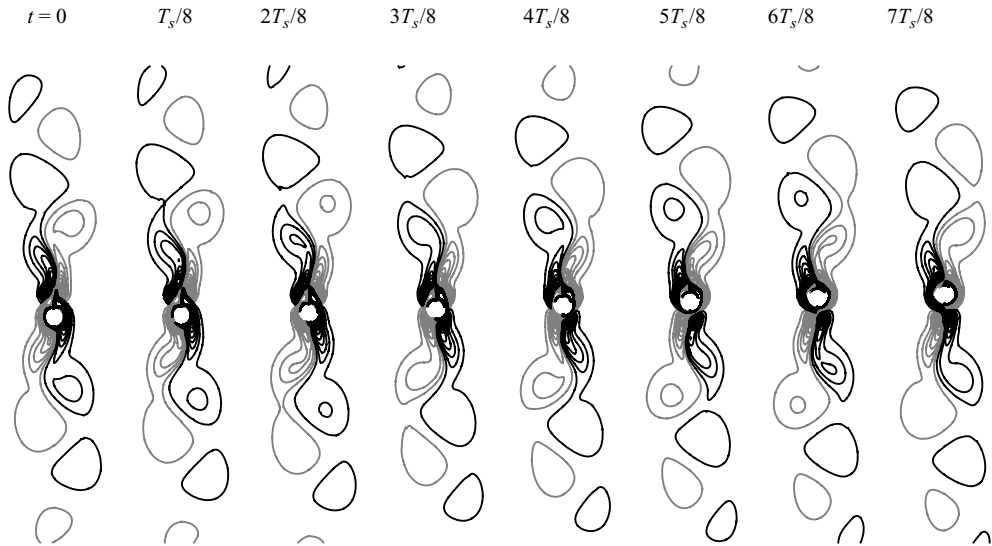


FIGURE 9. A sequence of instantaneous vorticity contours for the quasi-periodic two-dimensional flow of regime QP, computed at ($\beta = 40$, $KC = 4.7$), where $T_s/T = 15.6$, at eight phases of the secondary period T_s .

the imaginary part is equivalent in the following sense: at criticality, the imaginary part of the eigenfunction can be obtained from the real part by evolution with the linearized Navier–Stokes equations through $T_s/4$. The presence of both real and imaginary eigenfunction components enables the construction of Floquet modes that have an arbitrary starting phase with respect to the base flow, as required by the quasi-periodic nature of the flows.

Figure 9 shows instantaneous vorticity contours for two-dimensional saturated DNS at ($\beta = 40$, $KC = 4.7$), at eight phase points equispaced over secondary period T_s . This sequence emphasizes the shedding of discrete vortices into the planar Kármán jets emanating above and below the cylinder. It is interesting that while the far-field features of the flow have a great deal of regularity and an obvious identifiable period (T_s) this is completely uncoupled from cylinder oscillations at period T . Apparently the cylinder oscillation sets up the streaming jet flows which then buckle at their own inherent length and time scales. Note that the vortex shedding is also associated with the slow side-to-side ‘flapping’ of the V-shaped structure of the near-cylinder vorticity.

3.3. Linear and nonlinear behaviour beyond criticality

The root-locus behaviour of the Floquet multipliers for the quasi-periodic regime above the curve of marginal stability in (β , KC) space (figure 5a) is interesting. This is illustrated in figure 10(a), for Keulegan–Carpenter numbers increased above the critical value, at $\beta = 44.2$. A complex-conjugate pair of multipliers emerges from the unit circle in a Neimark–Sacker bifurcation at $KC_c = 4.52$, with associated secondary period $T_s \approx 13T$. With further increase in KC , the complex-conjugate pair approaches the real axis, and, at $KC_\infty = 4.678$, coalesce. From this point emerge two solution branches with real multipliers, one of which with further sufficient increase in KC re-enters the unit circle, the other proceeding further along the real axis, outwards along the real axis.

As coalescence is approached, $T_s \rightarrow \infty$, at least for linear modes. However, the behaviour obtained from nonlinear solutions (DNS) can differ. In figure 10(b) we see the ratio T_s/T obtained from linear analysis (thin solid line) compared to the value

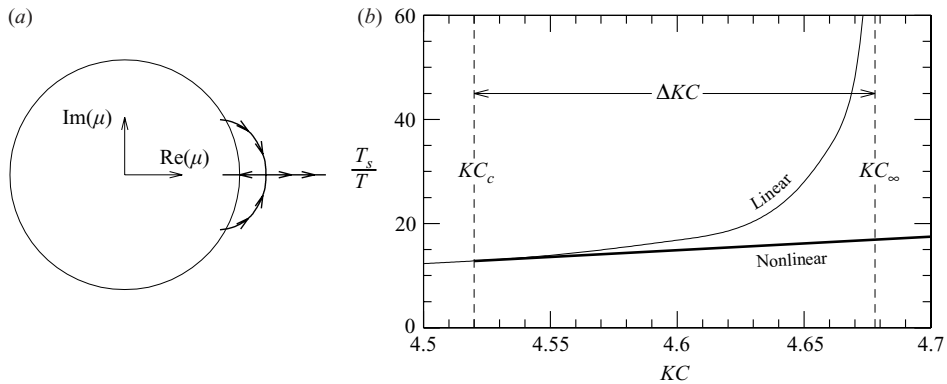


FIGURE 10. Coalescence of solution branches for regime QP, $\beta = 44.2$. As KC is increased, a complex-conjugate pair of multipliers emerges from the unit circle in the complex plane, as shown in the root locus of (a). With further increase in KC , the pair approaches the real axis, then coalesce. In (b) of the ratio T_s/T obtained from linear analysis (thin solid line) is compared with results obtained via two-dimensional DNS (thick solid line).

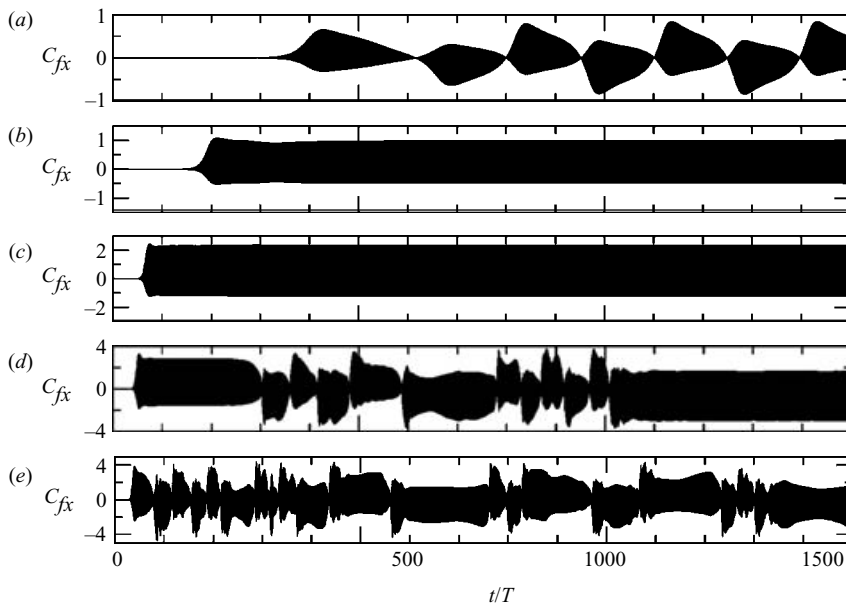


FIGURE 11. Time series of coefficients of force normal to the oscillation axis for two-dimensional flows at $KC = 7$. (a) $\beta = 13.5$; (b) $\beta = 13.75$; (c) $\beta = 15$; (d) $\beta = 16$; (e) $\beta = 17.5$.

obtained via Fourier analysis of velocity time series from a sequence of DNS solutions (thick solid line). At linear onset, the linear and nonlinear frequency ratios agree, while with increasing KC , the value of T_s/T obtained from DNS remains bounded, out to values beyond KC_∞ . This means that the nonlinear solutions can maintain their quasi-periodic solution branch through the linear coalescence. The increment in KC required to produce coalescence, ΔKC , increases with Stokes number, while at the ‘freezing point’, $\Delta KC = 0$.

On the other hand, the initial effect of parameter variation does not necessarily determine behaviour remote from the primary bifurcations. In figure 11 we show a set

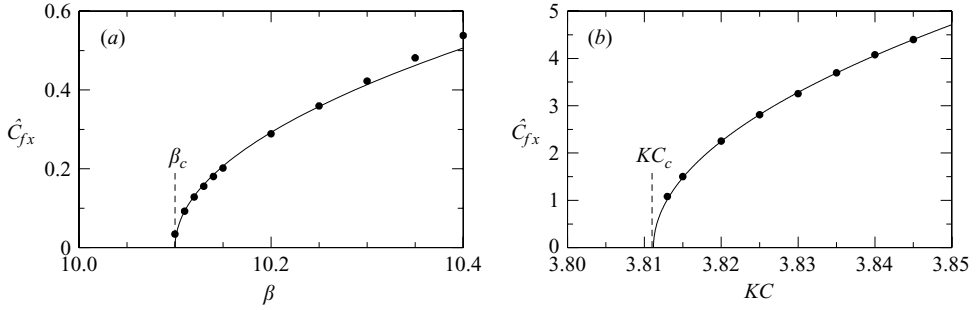


FIGURE 12. Bifurcation diagrams for two-dimensional symmetry breaking, showing coefficients of peak x -component force as functions of bifurcation parameter: (a) bifurcation to regime S at $KC = 8$; (b) bifurcation to regime QP at $\beta = 80$.

of time series of coefficients of force in the x -direction, i.e. normal to the oscillation axis, for simulations started from rest. These results were produced at $KC = 7$, with Stokes numbers $\beta = 13.5\text{--}17.5$, greater than β_f , so we predict the initial behaviour to be quasi-periodic. According to the regime map of Tatsuno & Bearman (1990, see figure 3) however, these control parameters all lie within synchronous regime D, with reported extent from $\beta \approx 13$ to $\beta \approx 20$ at $KC = 7$. Figure 11(a), for $\beta = 13.5$, shows that after symmetry breaks, the asymptotic behaviour is quasi-periodic, with $T_s/T \approx 200$. However, at $\beta = 13.75$ and 15, (figure 11b, c), the asymptotic results are flows in regime S, with time-mean non-zero values of C_{fx} , becoming larger with increasing β . The progression from quasi-periodic to synchronous behaviour at the same oscillation amplitude is possible because the control space is two-dimensional. Note also that the parameter values for figures 11(b) and 11(c) are respectively identical to those in figures 6 and 7, used to illustrate regime S. Then, as seen in figure 11(d, e), further increase in Stokes number produces intermittent switching behaviour, akin to (three-dimensional) flows in Tatsuno & Bearman's regime E.

To close the investigation of two-dimensional symmetry breaking, we turn now to the nonlinear properties of the primary bifurcations comparatively remote from the freezing point. Sample bifurcation diagrams for the transitions to regimes S and QP are shown in figure 12, where in each case one control parameter has been held fixed, and the other varied, producing codimension-1 projections of the possible codimension-2 bifurcations. The measure of energy in the solution is the peak force coefficient in the x -direction, \hat{C}_{fx} . In each case, the measure departs from zero without jump discontinuity as the critical bifurcation parameter is passed; the bifurcations are both supercritical. Consequently the related flows depart increasingly from K_x -symmetry as distance from the marginal curve increases (as can be seen e.g. by comparison of figures 6 and 7, and in agreement with figure 11b, c), but this increase cannot be maintained indefinitely – we suggest that a breakdown of the trend leads to the switching behaviour seen in figure 11(d, e) and in the three-dimensional flows of regimes E, F and G.

4. Three-dimensional symmetry breaking

When considering three-dimensional ($O(2)$) symmetry breaking, an additional parameter, the spanwise wavelength λ or equivalently wavenumber $k = 2\pi D/\lambda$, must be introduced to characterize the instability modes. From the two-dimensional analysis of §3 we know that two-dimensional symmetry breaking may be a precursor to

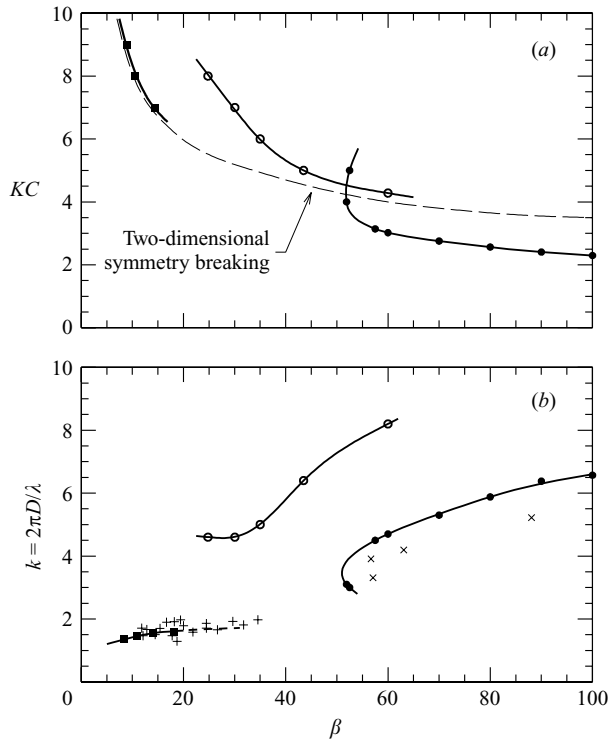


FIGURE 13. Marginal stability curves for three-dimensional modes. For data labelled \bullet , \circ , the base flow had two-dimensional reflection symmetry, and respectively the three-dimensional modes have H_1 and H_2 spatio-temporal symmetry at any z . For data labelled \blacksquare , the base flow had broken two-dimensional symmetry. In (a), the curve of two-dimensional symmetry breaking from figure 5(a) is shown. In (b), wavenumber data from Tatsuno & Bearman (1990) are represented by \times (regime B) and $+$ (regime D).

three-dimensional instabilities in some regimes, and there is a choice of either, as in §3, using two-dimensional base flows with imposed K_x reflection symmetry, or using states that have already broken symmetry. It also known from our two-dimensional analysis in combination with the experimental observations of Tatsuno & Bearman (1990) that the transition $A^* \rightarrow B$ occurs at Keulegan-Carpenter numbers below the onset of two-dimensional symmetry breaking. Finally, while Floquet analysis can be used to study the three-dimensional stability of periodic regimes A, A^* , B and D, it cannot be applied to quasi-periodic regime C (or two-dimensional regime QP) – here we must resort directly to DNS.

The marginal stability data for three-dimensional modes are summarized in figure 13. In figure 13(a), the line of marginal stability for two-dimensional symmetry breaking has been taken from figure 5(a); for all (β, KC) above this line the flows are liable to break two-dimensional symmetry before the onset of three-dimensional instability. In order to follow stability boundaries above this transition in our Floquet analysis, we may employ base flows which are constrained to be K_x -symmetric (as for the two-dimensional analysis). It can be seen that in this case there are two curves of marginal three-dimensional stability that cross or lie above the two-dimensional transition curve. These two modes can be differentiated by their two-dimensional spatio-temporal symmetries: the mode whose curve crosses the

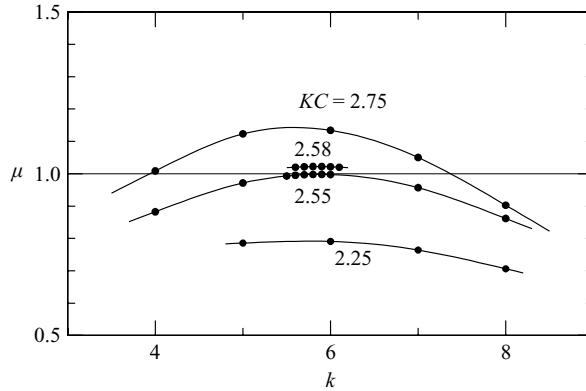


FIGURE 14. Floquet multipliers as functions of wavenumber and Stokes number for the three-dimensional instability of regime B at $\beta = 80$.

two-dimensional transition from below has symmetry H_1 at any z -location, while the other has symmetry H_2 . As will later be demonstrated in figure 24, the lower curve generally agrees very well with the A*–B transition boundary established by Tatsuno & Bearman (1990), and the experimental observations (see figure 3) suggest that the flows of regime B have H_1 symmetry at any z -location. We shall return to give more detailed treatment to the regime B instability in §4.1.

For base flows with broken two-dimensional symmetry, it is found from both Floquet analysis and three-dimensional DNS studies that the flows of two-dimensional regime S are almost immediately unstable to three-dimensional perturbations, and that the bifurcations are supercritical, as are the underlying two-dimensional cases. Hence the data for marginal three-dimensional stability of regime S lie very close to the two-dimensional transition curve. More detail of the three-dimensional instability of regime D is supplied in §4.2. For two-dimensional regime QP, the quasi-periodic nature of the base flows precludes Floquet analysis. In order to study three-dimensional stability of these flows, we have used DNS to investigate three-dimensional instability, at a single Stokes number, $\beta = 40$. This work will be described in §4.3.

Wavenumbers for the most unstable three-dimensional modes, corresponding to the data of figure 13(a), are presented in figure 13(b). Here it is seen that the branches for the instabilities of base flows with enforced symmetry, which intersect near $\beta = 50$ in figure 13(a), are quite remote in (β, k) space. Experimental measurements of wavenumber from Tatsuno & Bearman (1990) for regimes B and D are in reasonable agreement with the computed critical wavenumber values.

4.1. Synchronous regime B – a primary instability

Here we will concentrate on the bifurcations for the lower branch shown in figure 13(a) where the two-dimensional symmetry of the base flows does not need to be artificially preserved. These three-dimensional flows of regime B are synchronous with the cylinder oscillation, no new temporal frequencies are introduced at the bifurcation, and the saturated state reached in DNS is completely time-periodic. Since regime B solutions bifurcate directly from two-dimensional base states this is a primary bifurcation.

Figure 14 shows the progression with KC of Floquet multipliers as functions of spanwise wavenumber k , for Stokes number $\beta = 80$. By interpolation we have

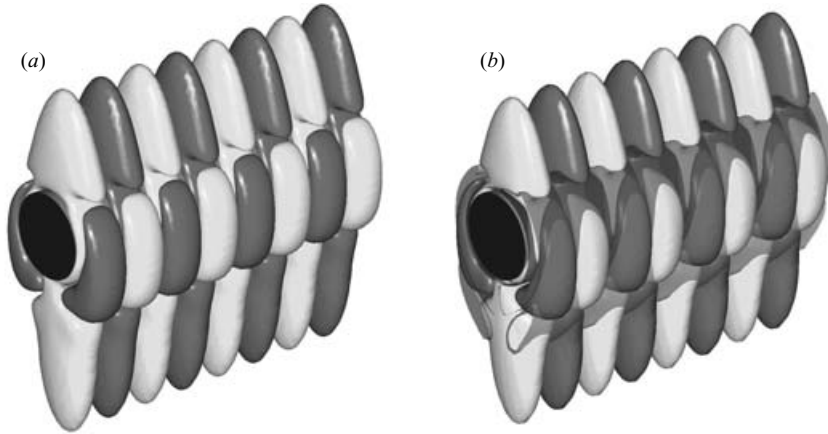


FIGURE 15. Instantaneous vorticity isosurfaces for the regime B instability at ($\beta=80$, $KC=2.58$, $k=5.88$), showing (a) the Floquet mode and (b) DNS result. Four spanwise repetitions are represented, at the instant when the cylinder is at y_{\max} . The solid isosurfaces show y -component vorticity of equal magnitude but opposite signs, while additionally in (b) translucent isosurfaces show z -component vorticity.

($KC_c=2.564$, $k_c=5.88$). A number of similar analyses were used to produce the critical-point data that are summarized in figure 13.

Figure 15 presents isosurface visualizations of the most unstable Floquet mode at ($\beta=80$, $KC=2.58$, $k=5.88$), together with those obtained from saturated DNS computed at the same location in control space. For the DNS, eight spanwise Fourier modes (16 real data planes) were employed to discretize a single spanwise wavelength; the figure shows four spanwise repetitions of the single simulated wavelength. From the shape and alignment of the isosurfaces of y -component vorticity in the Floquet mode above and below the cylinder – arrays of counter-rotating vortices – it might be expected that the main effect far from the cylinder would be to provide a spanwise wave to the flow, and one which has H_1 spatio-temporal symmetry at any spanwise location. This matches what has been observed in the experiments of Honji (1981) and Tatsuno & Bearman (1990). Evidently flow obtained through DNS is closely related to the Floquet instability mode. The main influence of nonlinear interaction on the three-dimensional instability is for vortex pairs to be drawn more closely together as they sweep past the shoulders of the cylinder, as can be determined through a detailed comparison of figures 15(a) and 15(b).

At any spanwise location, the sign of y -vorticity above and below the cylinder (and also at $\pm x$, for any y -location), is the same, but near the shoulder of the cylinder there is a change of sign of y -vorticity on a radial traverse. It appears that the y -vorticity at locations above and below the cylinder is generated on the cylinder surface, and is advected away from the cylinder by the oscillatory flow. The outer vorticity structures near the shoulder of the cylinder apparently remain in a broadly similar location relative to the cylinder over a motion cycle, and preserve their sense of spin. In figure 16 we show contours of kinetic energy in the first spanwise harmonic from the saturated DNS, plotted at $T/8$ increments. The energy is closely confined to the near-cylinder region, and the innermost structures which in figure 15 extend above and below the cylinder, all have the same sign of y -vorticity. It appears that, in agreement with the high- β asymptotic stability analysis of Hall (1984), the likely

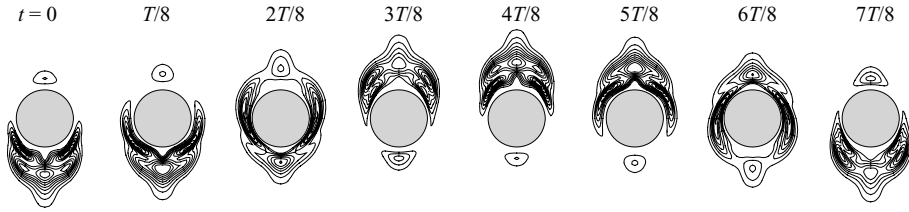


FIGURE 16. Contours of instantaneous kinetic energy in the fundamental spanwise harmonic for three-dimensional synchronous flow in regime B, obtained over one temporal period via saturated DNS at ($\beta = 80$, $KC = 2.6$, $k = 5.88$).

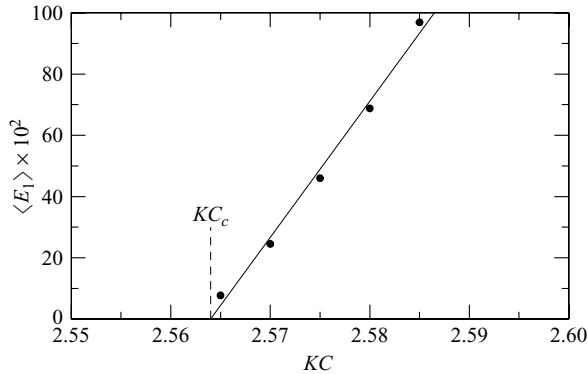


FIGURE 17. Bifurcation diagram for three-dimensional symmetry breaking in regime B, showing normalized time-average kinetic energy in the first spanwise harmonic, $\langle E_1 \rangle$ as a function of KC at $\beta = 80$, and $k = 5.88$. Values of E_1 are small because the normalization has the computational domain area in the denominator, while most of the three-dimensional energy is concentrated near the cylinder.

underlying mechanism for this mode is a centrifugal instability arising in the boundary layer flows as they sweep past the shoulder of the cylinder.

To examine the nonlinear properties of the bifurcation, we plot the normalized time-average kinetic energy in the fundamental spanwise harmonic $\langle E_1 \rangle$ from saturated DNS states at various Keulegan–Carpenter numbers above the critical value, at $\beta = 80$. The outcome appears in figure 17, and shows that the bifurcation is supercritical, also that the onset oscillation amplitude agrees well with the linear stability analysis (figure 14). Our finding of supercriticality disagrees with Hall (1984)’s suggestion that the bifurcation is subcritical in the high- β limit, although we note that there is no requirement for the nonlinear nature of a bifurcation (sub- or supercritical) to be invariant along the curve of marginal stability, and also that Hall was rather equivocal about his prediction.

4.2. Synchronous regime D – a secondary instability

The basic states for regime D are two-dimensional saturated states in regime S, which have broken two-dimensional symmetry. As for regime B, the three-dimensional flows of regime D are synchronous with the cylinder oscillation, and the saturated three-dimensional states found in our DNS are also limit cycles. The instabilities of regime D are of longer spanwise wavelength than those of regime B.

The progression of Floquet multipliers as functions of wavenumber with increasing Stokes number at $KC = 8$ is shown in figure 18. The two-dimensional analysis for

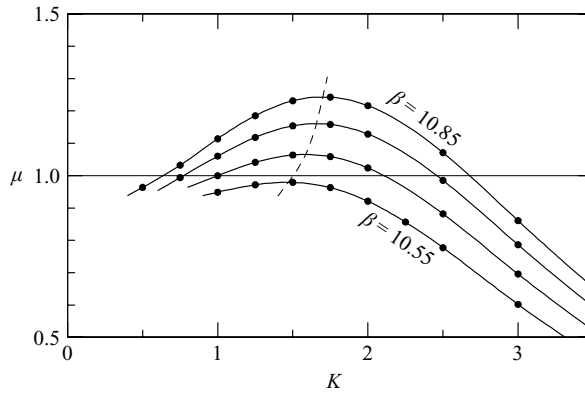


FIGURE 18. Floquet multipliers as functions of wavenumber and Stokes number for the three-dimensional secondary instability of regime D at $KC = 8$. The critical wavenumber $k_c = 1.51$ and $\beta_c = 10.58$. For comparison, the critical Stokes number for two-dimensional symmetry breaking at the same oscillation amplitude is $\beta = 10.1$.

regime S at the same oscillation amplitude gave $\beta_c = 10.1$, whereas here in the three-dimensional case, $\beta_c = 10.58$, with $k_c = 1.51$. Evidently a small but finite departure from two-dimensional symmetry is required to trigger the secondary three-dimensional instability.

Instantaneous vorticity isosurfaces for the leading Floquet mode and for DNS at ($\beta = 14.15$, $KC = 7$, $k = 1.75$) are shown in figure 19. In this case, 16 spanwise Fourier modes have been used to resolve a single wavelength of the DNS, and the visualizations show three spanwise repetitions. The broken two-dimensional symmetry is immediately evident. The Floquet mode (and so too, the DNS result) preserves the H_1 symmetry of the regime S basic state. Again, as for regime B, when comparing figures 19(a) and 19(b), the influence of nonlinear interaction appears to result in a closer spanwise coupling of pairs of y -oriented vortices than is apparent for the Floquet mode.

Compared to regime B, the mechanism of vorticity production and transport for regime D is more complicated. It retains the feature that at any spanwise location the sign of y -vorticity that advects far away from the cylinder agrees with that generated at the cylinder surface, and is opposite that which appears most prominent near the shoulder of the cylinder in figure 19. In figure 20 we plot a sequence of contours of kinetic energy in the first spanwise Fourier mode. Again it appears likely that the three-dimensional structure of regime D results from a centrifugal instability, re-energized in each sweep past a (in this case, principally a single) shoulder of the cylinder.

The bifurcation and nonlinear characteristics of mode D are examined in figure 21, which (as for figure 17) shows the dependence of the time-average normalized kinetic energy in the first spanwise mode on a bifurcation parameter, in this case β . As for regime B, the bifurcation is supercritical. Note again the margin in β between the onset of two-dimensional and three-dimensional symmetry breaking, and that the Stokes number of the bifurcation agrees with the outcome of the Floquet analysis (figure 18).

4.3. Quasi-periodic regime C

The quasi-periodic two-dimensional flows of regime QP are not amenable to three-dimensional Floquet analysis, so instead we have employed DNS, which has considerably greater computational expense. Consequently the scope of the

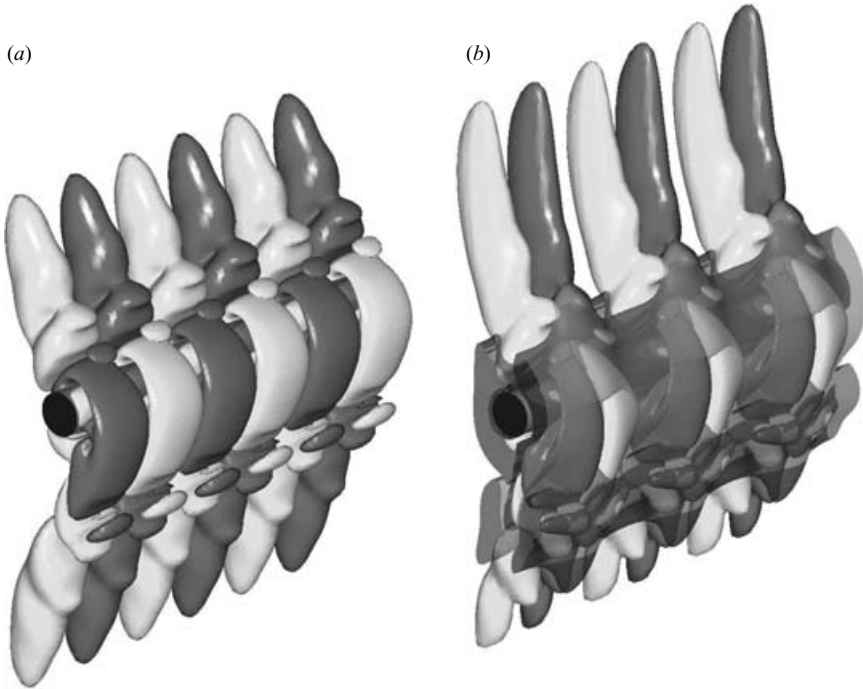


FIGURE 19. Instantaneous vorticity isosurfaces for the regime D instability at ($\beta = 14.15$, $KC = 7$, $k = 1.75$), showing (a) the Floquet mode and (b) DNS result. Three spanwise repetitions are represented, at the instant when the cylinder is at y_{\max} . The solid isosurfaces show y -component vorticity of equal magnitude but opposite signs, while additionally in (b) translucent isosurfaces show z -component vorticity.

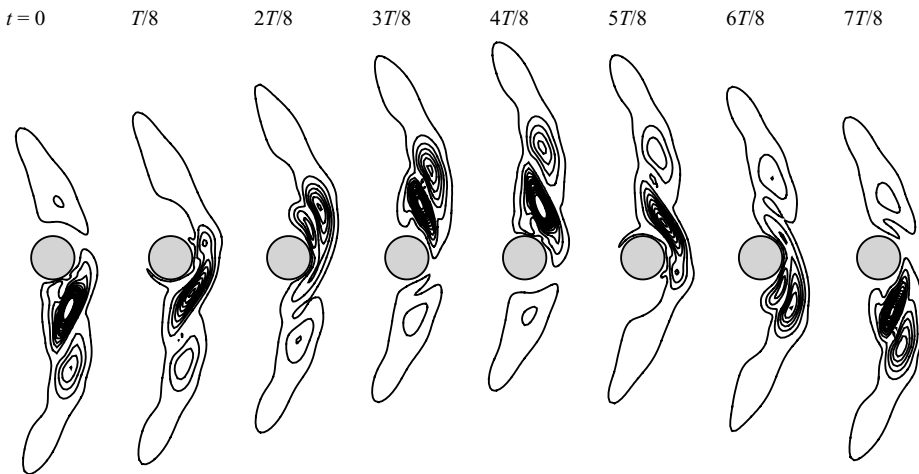


FIGURE 20. Contours of instantaneous kinetic energy in the fundamental spanwise harmonic for three-dimensional synchronous flow in regime D, obtained over one temporal period via saturated DNS at ($\beta = 14.15$, $KC = 7$, $k = 1.75$).

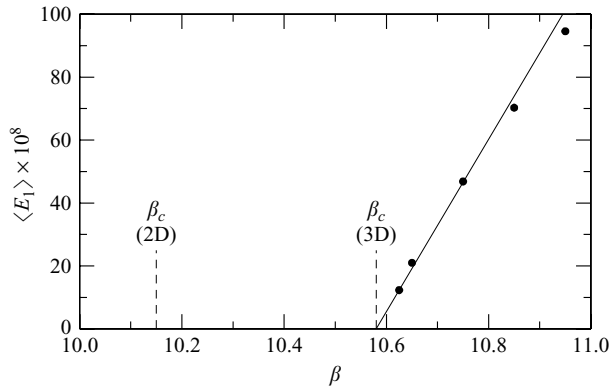


FIGURE 21. Bifurcation diagram for three-dimensional symmetry breaking in regime D, showing normalized time-average kinetic energy in the first spanwise harmonic, $\langle E_1 \rangle$ as a function of β at $KC = 8$, $k = 1.55$. Also indicated is the Stokes number for two-dimensional symmetry breaking at the same oscillation amplitude.

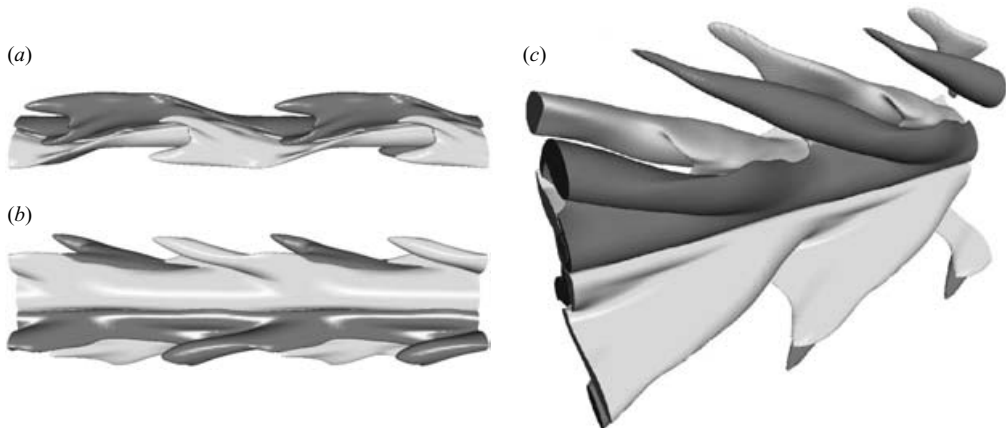


FIGURE 22. Instantaneous vorticity isosurfaces for the regime C instability, obtained from DNS at $(\beta = 40, KC = 4.8, k = 0.5)$. Two spanwise repetitions of equal-magnitude positive and negative isosurfaces of spanwise vorticity component are shown: (a) top; (b) side and (c) perspective views. Isosurface magnitudes in (c) are lower than for (a, b).

investigation here is more restricted than in §§4.1 and 4.2, and we have limited attention to a single Stokes number, $\beta = 40$, which lies between the lower transition value $\beta_f \approx 12$ (see figure 5), and $\beta \approx 50$, the lower limit of regime B (figure 13). Our initial work (not reported here in detail) consisted of a (β, KC) -space investigation in which the three-dimensionality was represented by a single spanwise mode. The results suggested that mode QP is initially unstable to a band of wavenumbers that emanate from $k = 0$, i.e. as perturbations of two-dimensional flow, and then, with slight increase in KC , to another band of wavenumbers centred around $k = 2$.

Subsequently we have carried out DNS at $(\beta = 40, KC = 4.8, k = 0.5)$, which falls within the initial instability envelope (the perturbation of two-dimensional flow), with 32 spanwise Fourier modes. Isosurfaces of spanwise vorticity component for this simulation are presented in figure 22. In side view, the isosurfaces present an array of

chevron shapes that are suggestive of those obtained by dye visualization for regime C by Tatsuno & Bearman (1990, figure 15). Likewise, the top view is suggestive of their figure 16. From the perspective view of figure 22(c), it appears that the large-scale two-dimensional Kármán-jet vortices seen in figures 8 and 9 now depart the cylinder in slantwise fashion.

5. Discussion

5.1. Two-dimensional symmetry breaking

The observed bifurcations from base flows with full symmetry to two-dimensional flows of regimes S and QP exhibit a great deal of similarity to the transitions A–D and A–C noted by Tatsuno & Bearman (1990), although it appears that there is also a very slender margin in (β, KC) -space where the flows are only two-dimensionally unstable. In addition, it seems likely – from the good agreement between the locations of the two-dimensional – regime QP marginal stability curve and Tatsuno & Bearman’s B–E transition, see figure 5(a) – that a predominantly two-dimensional transition gives rise to regime E, even though the flows of regime B are already three-dimensional. This idea is given support by Tatsuno & Bearman’s description of regime E: the ‘flow pattern in this regime temporarily resembles that in regime D. The flow which convects to one side of the axis of oscillation, however, intermittently changes its direction to the other side’.

The change from regime QP to regime S along the marginal stability curve occurs at the codimension-2 ‘freezing point’, where secondary periods become unbounded and the critical complex-conjugate-pair Floquet multipliers coalesce at $\mu = +1$. After coalescence, bifurcations across the marginal stability curve correspond to a single real Floquet multiplier crossing the unit circle. The two-dimensional flows of A and A* can be thought of as limit cycles in an appropriate phase space. As discussed in §1.1, they have a $Z_2 \times Z_2$ symmetry group. The bifurcations to two-dimensional regimes S and QP appear to be analogous to the codimension-1 Z_2 -equivariant bifurcations discussed by Kuznetsov (1998, §7.4.4). For regime S, we have a pitchfork bifurcation at $\mu = +1$, leading to a K_x -conjugate pair of limit cycles. For regime QP, which arises through a Z_2 -equivariant Neimark–Sacker bifurcation, the bifurcation produces a 2-torus that has a Z_2 spatio-temporal symmetry group, inherited from the underlying limit cycle. In this case, we can infer from inspection of the particle-track image of figure 8(d) that the 2-torus has H_1 symmetry.

The behaviour of the quasi-periodic two-dimensional modes above the critical curve was presented in §3.3. Multipliers emerge from the unit circle in complex-conjugate pairs, but with further increase in bifurcation parameter, approach the real axis and coalesce, eventually leaving a single stable synchronous mode (see figure 10). As β increases, the increment ΔKC required to produce coalescence also increases. A scenario that is consistent with this behaviour is sketched in figure 23, where the (β, KC) -space is partitioned into two subdomains, one in which quasi-periodic modes are least stable, the other in which synchronous modes are least stable. Coalescence occurs along the boundary between the shaded and unshaded regions, which the curve of marginal stability (the contour $|\mu| = 1$) crosses at the ‘freezing point’. We note that the transition between regimes C and D recorded by Tatsuno & Bearman (1990) occurred at considerably higher Stokes number, and lower Keulegan–Carpenter number, ($\beta \approx 25, KC \approx 4.25$). However, this apparent discrepancy might be explained by a narrowing of the envelope in which mode QP is linearly unstable, with decrease in Stokes numbers towards β_f , as shown in figure 23. We note that the β -dependence

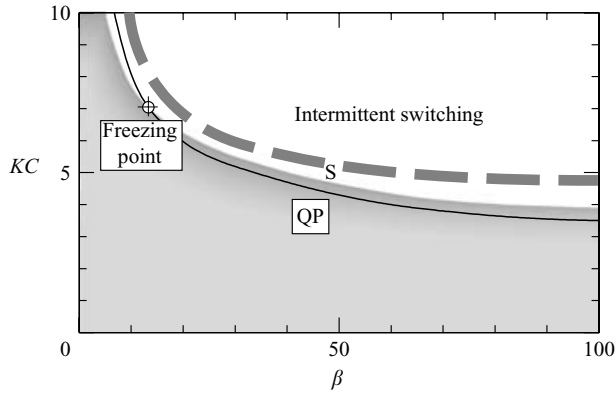


FIGURE 23. Scenario for partition of (β, KC) -space into two-dimensional linear synchronous and quasi-periodic regimes: complex-conjugate-pair multiplier coalescence occurs along the border between the shaded and unshaded regions. The solid line is the curve of marginal stability, the contour corresponding to $|\mu|=1$. The indistinct dashed line indicates the onset of intermittent switching brought about by nonlinear effects.

of two-dimensional DNS results at $KC = 7$ presented in figure 11(*a, b*) is consistent with the partition suggested in figure 23. A very fine-gridded parameter search may be needed to adequately resolve the boundary.

Other interesting possibilities arise because, as shown in figure 10(*b*), in the nonlinear case we can pass through the coalescence which occurs for the linearly unstable modes, but without change in regime, the extent of (β, KC) -space with quasi-periodic stable saturated states may be considerably more extensive than is indicated by the area of linear instability in figure 23. Near the codimension-2 freezing point, it may also be possible to obtain regime S or QP states at the same location in control space, depending on initial conditions.

Further from the curve of marginal stability however, nonlinear effects begin to be asserted more strongly. As explained in §3.3, flows become increasingly asymmetrical as their location in (β, KC) -space moves away from criticality, and ultimately this increase cannot be maintained. The outcome is the onset of intermittent two-dimensional switching behaviour as seen in figure 11(*d, e*), and previously documented to occur in at least the three-dimensional regimes E and G. We have not attempted to rigorously examine this nonlinear effect, but have indicated its onset in figure 23 as an indistinct dashed line.

In their three-dimensional simulation at $(KC = 6.5, \beta = 20)$ Nehari *et al.* (2004), nominally investigating regime D, reported that the flow, instead of maintaining a constant sign of broken two-dimensional symmetry as they expected from the work of Tatsuno & Bearman (1990), switched orientation intermittently from one side of the oscillation axis to the other. However, in two-dimensional simulations at the same location in (β, KC) -space, we have also found intermittent switching behaviour, like that of figure 11(*d, e*). Thus their simulation might be better categorized as being of regime E flow, rather than D.

At higher values of Keulegan–Carpenter number than employed here, other two-dimensional instability modes may be the primary instabilities. For example, the flows of our regime S have H_1 symmetry, and we know from the work of Tatsuno & Bearman (1990) that at higher Keulegan–Carpenter numbers and lower Stokes numbers the flows of regime F appear, superficially at least, close to being

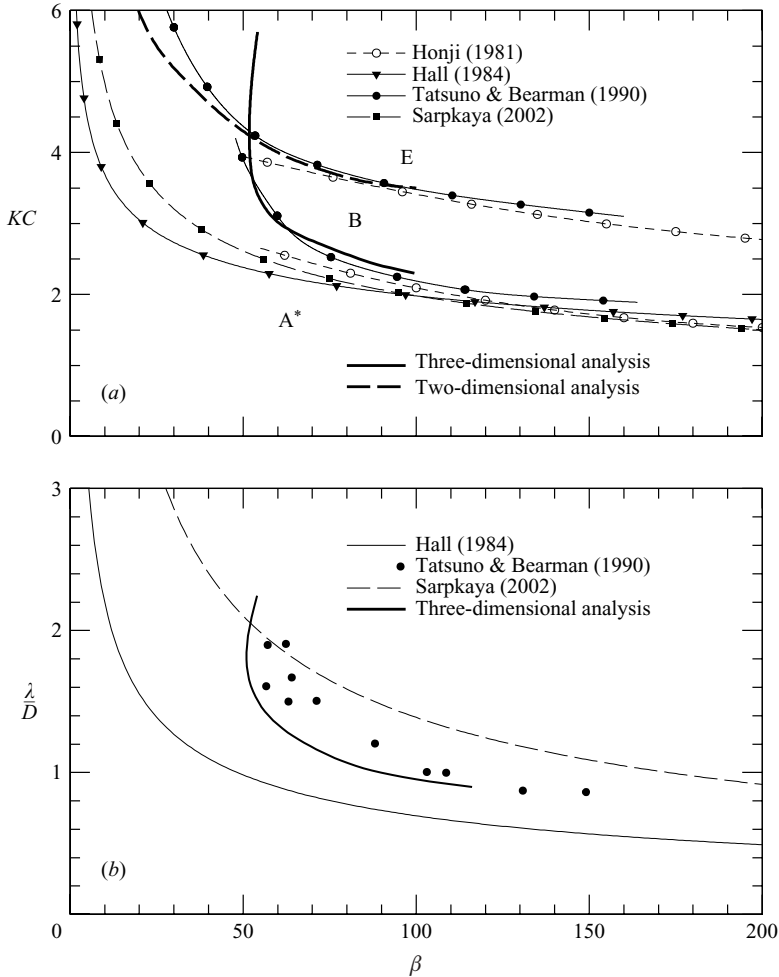


FIGURE 24. Comparison of previous results with those established via Floquet analysis. In (a), thin lines with symbols show (β, KC) marginal stability boundaries presented in previous experimental and theoretical studies (see legend), and thick lines those established in the present Floquet analysis. Labels A*, B, and E are the regime names given by Tatsuno & Bearman (1990). In (b), lines and symbols show wavelengths of the corresponding three-dimensional instabilities.

H_2 -symmetric. However, all the simulation results so far for (β, KC) -space locations lying in regime F (including our own preliminary work, not detailed here) have been non-synchronous. We may speculate that at higher KC -values along the marginal stability curve, another codimension-2 point could introduce a fully synchronous H_2 -symmetric two-dimensional mode analogous to regime F.

5.2. Three-dimensional symmetry breaking

A comparison of some previous experimental and analytical results with outcomes of our stability analysis, both two- and three-dimensional, appears in figure 24. Regarding the A*–B regime transition shown in figure 24(a), our curve of marginal stability agrees well with the regime boundary supplied by Tatsuno & Bearman (1990), with the experimental results of Honji (1981), and, towards the upper limit of the

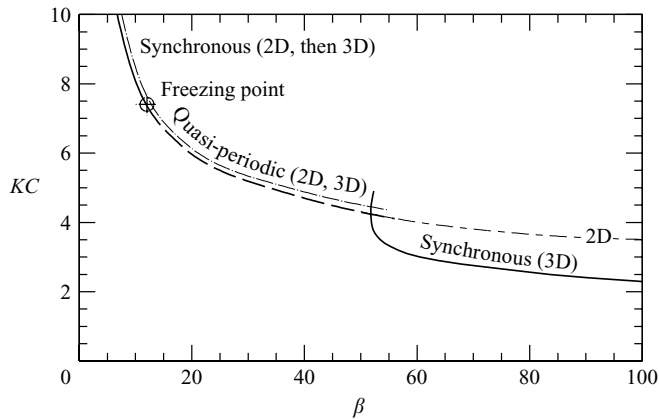


FIGURE 25. Locations and characteristics of the primary and secondary symmetry-breaking bifurcations.

Stokes numbers we have used, with the stability analysis of Hall (1984, here, equation (1.9)), as well as the correlation of Sarpkaya (2002, here, (1.11)). In figure 24(b), it can be seen that our predictions for spanwise wavelengths for this instability agree well with measurements by Tatsuno & Bearman, and that the wavelengths are intermediate between the correlation supplied by Sarpkaya (2002, here, (1.11)) and the high- β -asymptotic result of Hall (1984, here, (1.10)).

Regarding the transition B–E, it can be seen in figure 24(a) that, as stated before, our two-dimensional curve of marginal stability agrees very well with the regime boundary supplied by Tatsuno & Bearman, and also with the ‘upper curve’ of Honji (1981), from which we may surmise that they all mark the same events, and that the B–E transition is fundamentally a two-dimensional one.

For the transition to three-dimensional flows of regime D, we have shown that flows with broken two-dimensional symmetry (regime S) need to be established before secondary instability sets in, although the change in parameter values required may not be large – in fact, perhaps too small to be reliably established in experiments.

The three-dimensional flows of regime C seen in figure 22 are spanwise-travelling waves, superimposed on top of the quasi-periodic behaviour of the underlying two-dimensional flows of regime QP. Since these travelling waves break spanwise reflection symmetry, they come in K_z -conjugate pairs, and the isosurfaces of figure 22 represent one of the pair. What may be an interaction of two travelling waves of this kind can be seen in Tatsuno & Bearman (1990, figure 15), which shows, in transverse elevation, distinct chevron shapes of dye advected from the cylinder surface. Again we expect, from the fact that the two-dimensional symmetry breaking to regime QP is supercritical, that a finite degree of two-dimensional symmetry breaking is required before regime C can arise as a secondary instability – but we have not investigated this point.

6. Conclusions

The outcomes of our investigation are summarized in figure 25. Within the range of control parameters $\beta \in [0, 100]$, $KC \in [0, 10]$, there are two fundamentally different types of symmetry-breaking instability in this flow: two-dimensional and three-dimensional. Flows for which two-dimensional symmetry breaking is the primary instability

are almost immediately unstable to three-dimensional secondary instabilities, and these secondary regimes are the ones that have been observed in experiments, e.g. regimes C and D identified by Tatsuno & Bearman (1990). Like their underlying two-dimensional equivalents (regimes S and QP), regime D flows are synchronous with the forcing, while flows of regime C are quasi-periodic. There is also a direct primary breakage to three-dimensional instability at Stokes numbers $\beta \gtrsim 50$; this produces regime B flow, first reported by Honji (1981), analysed by Hall (1984), noted by Tatsuno & Bearman (1990) and most recently investigated experimentally by Sarpkaya (2002). This is another synchronous mode. On the basis of Sarpkaya's results, it further appears that for all $\beta \gtrsim 50$ this mode remains the first to be encountered as Keulegan–Carpenter numbers are increased from small values. The fundamental distinction between flows of regimes C and D, on the one hand, and those of regime B on the other, is that on the spanwise average flows of regime B have the two-dimensional symmetries of the base flows, while those of regimes C and D do not. At an arbitrary location z along the cylinder span, flows of all three regimes retain spatio-temporal symmetry H_1 and the remaining symmetry group is Z_2 . All the observed bifurcations (both two- and three-dimensional) are of supercritical type. Far from the curve of two-dimensional marginal stability, nonlinear effects produce intermittent switching behaviour, with the orientation of symmetry breaking shifting from one side of the oscillation axis to the other.

Finally, it should be reiterated that we have dealt only with the primary and secondary symmetry-breaking instabilities: there are a number of other cases to be considered, even within the parameter limits of this investigation. The detail of our findings, particularly regarding the distinction between synchronous, quasi-periodic, and intermittent switching behaviour, suggests that the regime map presented by Tatsuno & Bearman (1990), while a very good guide to the terrain to be encountered in such a study, is, like many early maps, to be interpreted with care.

We would like to thank M. Tatsuno and P. W. Bearman for their kind help in supplying images for figure 3. We wish to acknowledge the contributions made by F. Marques in discussions concerning the algebra of two-dimensional symmetry groups and symmetry breaking, and D. Barkley in helping us to resolve questions about stability analysis and dynamics. This research received support from both the Australian Partnership for Advanced Computing and the Victorian Partnership for Advanced Computing.

REFERENCES

- BARKLEY, D. & HENDERSON, R. D. 1996 Three-dimensional Floquet stability analysis of the wake of a circular cylinder. *J. Fluid Mech.* **322**, 215–241.
- BLACKBURN, H. M. & HENDERSON, R. D. 1999 A study of two-dimensional flow past an oscillating cylinder. *J. Fluid Mech.* **385**, 255–286.
- DÜTSCH, H., DURST, F., BECKER, S. & LIENHART, H. 1998 Low-Reynolds-number flow around an oscillating cylinder at low Keulegan–Carpenter numbers. *J. Fluid Mech.* **360**, 249–271.
- ELSTON, J. R., SHERIDAN, J. & BLACKBURN, H. M. 2004 Two-dimensional Floquet stability analysis of the flow produced by an oscillating circular cylinder in quiescent fluid. *Eur. J. Mech. B/Fluids* **23**, 99–106.
- GOLUBITSKY, M., STEWART, I. & SCHAEFFER, D. G. 1988 *Singularities and Groups in Bifurcation Theory: II*. Appl. Math. Sci., vol. 69. Springer.

- HALL, P. 1984 On the stability of the unsteady boundary layer on a cylinder oscillating transversely in a viscous fluid. *J. Fluid Mech.* **146**, 347–367.
- HONJI, H. 1981 Streaked flow around an oscillating cylinder. *J. Fluid Mech.* **107**, 509–520.
- ILIADIS, G. & ANAGNOSTOPOULOS, P. 1998 Viscous oscillatory flow around a circular cylinder at low Keulegan–Carpenter numbers and frequency parameters. *Intl J. Numer. Meth. Fluids* **26**, 403–442.
- IOOSS, G. & JOSEPH, D. D. 1990 *Elementary Stability and Bifurcation Theory*, 2nd edn. Springer.
- JUSTESEN, P. 1991 A numerical study of oscillating flow around a circular cylinder. *J. Fluid Mech.* **222**, 157–196.
- KARNIADAKIS, G. E. 1990 Spectral element–Fourier methods for incompressible turbulent flows. *Comput. Meth. Appl. Mech. Engng* **80**, 367–380.
- KARNIADAKIS, G. E., ISRAELI, M. & ORSZAG, S. A. 1991 High-order splitting methods for the incompressible Navier–Stokes equations. *J. Comput. Phys.* **97**, 414–443.
- KUZNETSOV, Y. A. 1998 *Elements of Applied Bifurcation Theory*, 2nd edn. Springer.
- NEHARI, D., ARMENIO, V. & BALLIO, F. 2004 Three-dimensional analysis of the unidirectional oscillatory flow around a circular cylinder at low Keulegan–Carpenter and β numbers. *J. Fluid Mech.* **520**, 157–186.
- OBASAJU, E. D., BEARMAN, P. W. & GRAHAM, J. M. R. 1988 A study of forces, circulation and vortex patterns around a cylinder in oscillating flow. *J. Fluid Mech.* **196**, 467–494.
- SARPKAYA, T. 1986 Force on a circular cylinder in viscous oscillatory flow at low Keulegan–Carpenter numbers. *J. Fluid Mech.* **165**, 61–71.
- SARPKAYA, T. 2002 Experiments on the stability of sinusoidal flow over a circular cylinder. *J. Fluid Mech.* **457**, 157–180.
- TATSUNO, M. 1973 Circulatory streaming around an oscillating circular cylinder at low Reynolds numbers. *J. Phys. Soc. Japan* **35**, 915–920.
- TATSUNO, M. 1981 Secondary flow induced by a circular cylinder performing unharmonic oscillations. *J. Phys. Soc. Japan* **50**, 330–337.
- TATSUNO, M. & BEARMAN, P. W. 1988 Visual study of the flow induced by a cylinder performing sinusoidal oscillations. *Bulletin* 66. Research Institute for Applied Mechanics, Kyushu University.
- TATSUNO, M. & BEARMAN, P. W. 1990 A visual study of the flow around an oscillating circular cylinder at low Keulegan–Carpenter numbers and low Stokes numbers. *J. Fluid Mech.* **211**, 157–182.
- TUCKERMAN, L. S. & BARKLEY, D. 2000 Bifurcation analysis for timesteppers. In *Numerical Methods for Bifurcation Problems and Large-Scale Dynamical Systems* (ed. E. Doedel & L. S. Tuckerman), pp. 453–566. Springer.
- VAN DYKE, M. 1982 *An Album of Fluid Motion*. Parabolic Press.
- WILLIAMSON, C. H. K. 1985 Sinusoidal flow relative to circular cylinders. *J. Fluid Mech.* **155**, 141–174.
- YANG, Y. & ROCKWELL, D. 2002 Wave interaction with a vertical cylinder: Spanwise flow patterns and loading. *J. Fluid Mech.* **460**, 93–129.
- YANG, Y. & ROCKWELL, D. 2004 Interaction of a deep-water wave with a circular cylinder: Flow structure and loading. *J. Fluid Mech.* **520**, 267–295.